

Evolution of microstructure, phases and mechanical properties in lean as-cast Mg–Al–Ca–Mn alloys under the influence of a wide range of Ca/Al ratio

S. Sanyal^{a,*}, M. Paliwal^b, T.K. Bandyopadhyay^a, S. Mandal^a

^a Department of Metallurgical and Materials Engineering, Indian Institute of Technology Kharagpur, Kharagpur, 721302, India

^b Materials Science and Engineering, Indian Institute of Technology, Gandhinagar, 382355, Gujarat, India



ARTICLE INFO

Keywords:

Mg alloy
Solute strengthening
Phase evolution
Thermodynamic calculations
Mechanical properties

ABSTRACT

In the present investigation, the microstructure and phase evolution, and their implications on the mechanical properties for different Ca/Al ratios (within ~0.06–2.21, wt.%) in lean as-cast Mg–Al–Ca–Mn alloys are experimentally studied. Further, the evolution of the second phases and the matrix phase in different alloy compositions have been estimated through thermodynamic calculations using Scheil conditions. The primary phase in all these alloys is a solid solution of hcp Mg with the other elements like Al and Ca. Apart from the fine Al_3Mn_5 particles present in all the compositions, the major eutectic second phase is $\gamma\text{-Mg}_{17}\text{Al}_{12}$ in the specimen with Ca/Al ratio ~0.06, C36-(Mg,Al)₂Ca in the specimen with Ca/Al ratio ~0.28 and C14-Mg₂Ca in the specimens with Ca/Al ratio ~1.56 and ~2.21. The area fraction of the eutectic second phases increases from ~2.1 to ~7.2% with the Ca/Al ratio, with a concomitant increase in its network connectivity as confirmed through fractal analysis. Contrarily, the lattice parameters (both *a* and *c*) and the elastic modulus (*E*) of the matrix phase decrease with increasing Ca/Al ratio, due to the decreasing concentration of solute atoms in the matrix. Therefore, the specimen with the minimum Ca/Al ratio (~0.06) attains maximum strength (YS ~130 MPa, UTS ~183 MPa), primarily owing to solid solution strengthening from higher solute content and precipitation strengthening from fine $\gamma\text{-Mg}_{17}\text{Al}_{12}$ particles. The large fraction and strong networks of hard and brittle Mg₂Ca phase promote cracks during tensile deformation and deteriorates the ductility ($\leq 1.6\%$) and work hardening response in the alloys with higher Ca/Al ratios (≥ 1.56).

1. Introduction

The Mg–Al–Ca–Mn alloy is one of the new generation Mg-based alloy systems, that shows promising results in terms of both ease of processing and mechanical properties [1–6]. These alloys are of particular interest for automobile components to be used in elevated temperatures, because of their ability to maintain good mechanical properties originating from the high thermal stability of Ca-rich phases [7–9]. However, despite the high thermal stability of the constituent phases [10–12] and additional weakening of the basal texture [11,13–18], the as-cast Ca-containing Mg-based alloys suffer from poor room temperature mechanical performance. It is suspected that the hard and brittle Ca-rich phases *viz.* Mg₂Ca, Al₂Ca, and (Mg,Al)₂Ca, are the possible reason behind such deterioration of room temperature mechanical properties [12]. However, it remains unclear exactly how each of these individual phases

affects the mechanical behavior in Mg–Al–Ca–Mn alloys.

The evolution of phases in the Mg–Al–Ca alloy system is reportedly governed by various compositional aspects such as the Al content [12, 19–21], Ca content [12,22,23] and Ca/Al content ratio [22–25] in the alloy composition. The common finding from these studies is that the dominating second phase changes from A12-Mg₁₇Al₁₂ (also referred to as the γ or β phase in some studies) and/or C15-Al₂Ca to C36-(Mg, Al)₂Ca to C14-Mg₂Ca as the Ca/Al content ratio increases in the alloy composition [10,12,20,22,24–26]. However, the content of the individual alloying elements as well as Ca/Al ratio in the composition determines the type, morphology, size, and fraction of these phases. Zhang et al. [20] have studied the second phase evolution in as-cast and hot extruded Mg–Al–Ca alloys with Ca/Al ratio varied from 0.4 to 1 (wt.%). Similarly, Li et al. [24] have also studied the microstructure evolution in both cast and hot extruded Mg–Al–Ca–Mn alloys, albeit for a much

* Corresponding author.

E-mail address: souriddha.sanyal@iitkgp.ac.in (S. Sanyal).

wider range of 0.25–1.3 (wt.%) of Ca/Al ratio. While both of these studies observed an overall improvement of mechanical properties with decreasing Ca/Al ratio in hot-extruded condition, none of them discussed the impact of the microstructural evolution on the mechanical properties in as-cast condition [20,24]. In this context, it is important to note that some of the final automobile components are cast and put to service after little or no machining. Therefore, attaining adequate properties and studying the structure-property relationship in as-cast alloys is essential for further development of these alloys. Elamami et al. [22] have studied the room temperature as well as elevated temperature mechanical properties in as-cast Mg-Al-Ca-Mn alloys. They have reported an increment in the hardness, room temperature strength and elevated temperature creep resistance with increasing Ca/Al ratio, with simultaneous deterioration in room temperature ductility [22]. However, the observations in this study are restricted to a small range of Ca/Al wt.% ratio (0.58–0.91), which possibly has led to the fairly marginal variations in the properties. Therefore, a systematic investigation on the microstructural evolution and subsequently, its effects on the room temperature mechanical properties for a wide-range of Ca/Al content ratio in as-cast Mg-Al-Ca-Mn alloys would be beneficial for holistic design and development of this alloy system.

In the present study, few novel lean compositions (total concentration of alloying elements within 4 wt%) in the Mg-Al-Ca-Mn alloy system have been designed and developed using a cost-effective permanent mold casting technique. The Ca/Al content ratio in the alloy compositions is varied between 0.06 and 2.21 (wt.%). The objectives of the study include investigating the implications of the varying Ca/Al content ratio on the microstructure and phase evolution of the as-cast alloys. Secondly, the mechanical properties of these as-cast alloys are evaluated and correlated with the microstructural developments. In addition, a thermodynamic database is developed for the Mg-Al-Ca-Mn alloy system by incorporating the respective binaries and important ternary systems. The thermodynamic calculations based on this database is used in explaining the as-cast phase evolution.

2. Experimental procedure

2.1. Alloy development

Pure Mg (98%), Al (99.5%), and Ca (99%) were melted along with MnCl₂ salt in a graphite crucible at 1023 K. Mixtures of MgCl₂, MnCl₂, CaF₂, and NaF salts were used as bottom as well as cover fluxes. The entire melting procedure for each alloy was carried out in an electrical resistance furnace. After melting, the molten alloys were poured in a preheated (523 K) stainless steel mold and subsequently air-cooled. The four different compositions prepared in this study and the nomenclature used henceforth for these alloys are listed in Table 1.

2.2. Mechanical testing

The microhardness (Vickers) tests were carried out with the help of a diamond indenter under 1 N (~100 g-f) load with 10 s dwell time in ANTON-PAAR Microindentation Tester (MHT³). The nano-indentation tests were carried out in Hysitron TI 950 TribolIndenter using a Berkovich indenter under 5 mN (~0.5 g-f) load with 10 s dwell time. A universal testing machine (INSTRON-3365) has been used to test the room

temperature tensile properties of the alloy specimens with 0.75 mm/min cross-head velocity (10^{-3} s⁻¹ initial strain rate). The flat tensile specimens were prepared by proportionately scaling down the ASTM B-557 M standard for a 12.5 mm gauge length.

2.3. Microstructural characterization

The alloy compositions in Table 1 were analyzed with the help of X-ray fluorescence spectroscopy in a Bruker S8 Tiger instrument. The grain size was measured through optical microscopy in a ZEISS AxioScope.A1 MAT microscope. The phases in all the alloys were analyzed by the X-ray diffraction (XRD) technique in a BRUKERS D8 Advance instrument, attached with a Cu-K α target. The 2θ ranges were set between 20° and 90° with 0.02° step-size. Phase identification in raw XRD data was performed using the X'Pert HighScore Plus software and ICDD PDF4 database. Lattice parameters of the matrix phase were estimated from the peak broadening in XRD profiles using Cohen's method [27,28]. The phases in the as-cast alloys, along with their fracture behavior, were further studied under a scanning electron microscope (ZEISS-Merlin Gemini 2 FESEM), attached with energy-dispersive X-ray spectroscopy (EDS). The as-cast specimens for optical microscopy and SEM analysis were prepared according to standard metallographic methods and subsequently etched in acetic picral solution [29,30]. The images obtained through SEM were analyzed in ImageJ software to estimate the second phase fractions and grain size. Fractal analysis was conducted on multiple SEM images for each alloy specimen to assess the connectivity of the second phase networks. Each SEM image was converted to binary and the largest mass cluster (D_{max}) was reconstructed from the second phases using a connected-component labeling algorithm [31]. The self-similar nature of D_{max} facilitates the estimation of fractal dimension (D_f) using the box-counting method [32–36]. The total number of boxes with edge length x (i.e. $N(x)$) required for complete coverage of the D_{max} could be expressed by the following equation,

$$N(x) = x^{-D_f} \quad (1)$$

Furthermore, the dislocation-particle interaction in the tensile-tested specimen was studied using high-resolution transmission electron microscopy (HRTEM) in a JEOL JEM2100F FEG-TEM. The specimen for this analysis was prepared by thinning to ~60 μm thick foil, followed by punching out 3 mm disc and finally ion milling in a Gatan Precision Ion Polishing unit. Precise composition analysis of the second phase is conducted using a three-dimensional atom probe (3DAP) in a CAMECA LEAP 5000 XR instrument operated in laser mode, with 200 kHz laser pulse frequency and 30 pJ focus laser energy. Specimens for 3DAP were prepared in a HELIOS Dual Beam SEM with the help of a focused ion beam (FIB). The reconstruction and analysis of the acquired 3DAP data were carried out using the IVAS (Version 3.8.2) application package of CAMECA.

2.4. Thermodynamic calculations

The thermodynamic calculations for the Mg-Al-Ca-Mn system were performed using FactSage software [37]. Thermodynamic database of the Mg-Al-Ca-Mn system was constructed through a combination of optimized thermodynamic parameters, for both solution phases and compounds, of the following binary systems: Mg-Al [38], Mg-Ca [39],

Table 1

Chemical composition of the as-cast alloys with Ca/Al content ratio in both wt.% and at.%

Alloy specimens	Major alloying elements (in wt.%)						Ca/Al ratio	
	Mg	Ca	Al	Mn	Si	Others	in wt.%	in at.%
CA0.0	98.20	0.05	0.87	0.57	0.18	Bal.	0.06	0.04
CA0.5	98.54	0.28	1.00	0.13	0.05	Bal.	0.28	0.19
CA1.5	96.70	1.28	0.82	0.44	0.17	Bal.	1.56	1.04
CA2.0	96.75	1.66	0.75	0.42	0.10	Bal.	2.21	1.5

Mg-Mn [40], Al-Ca [41], Al-Mn [42], Ca-Mn [43] and ternary systems: Mg-Al-Ca [44] and Mg-Al-Mn [42]. The liquid and hcp Mg phase were modeled using a regular solution model whereas phases such as C14, C15, and ternary Laves phase were described using a Compound Energy Formalism (CEF) framework.

3. Results

3.1. Microstructure studies

3.1.1. Evolution of grain size

Fig. 1 illustrates the optical microscopy images showing the grain structures in the studied alloys. Due to the large variations in the grain sizes, the optical images presented in **Fig. 1(a-d)** were obtained at different magnifications. The CA0.0 specimen shows extremely large grains and hence, separate images were stitched together to present a low magnification image in **Fig. 1(a)**. The grains are slightly less coarse in the CA0.5 specimen (**Fig. 1(b)**), as compared to the CA0.0 specimen (**Fig. 1(a)**). Significant reduction in grain size and increment in the amount of second phases can be observed in both CA1.5 (**Fig. 1(c)**) and CA2.0 specimens (**Fig. 1(d)**). The grain structure in the latter specimen appears to be slightly dendritic in nature (**Fig. 1(d)**). The grain size of each specimens was estimated from **Fig. 1** using the linear intercept method and presented in **Table 2**. Evidently, the average grain size is the largest in CA0.0 specimen and it decreases with increasing Ca/Al content ratio. The standard deviation (SD) values, presented in the form of uncertainty in **Table 2**, reflect the significantly larger inhomogeneity in the distribution of grain size in the CA0.0 specimen, in comparison to the other three specimens.

3.1.2. Distribution of the second phases

The SEM images in **Fig. 2**, exhibit the distribution of the second phases in all the alloy specimens. The CA0.0 specimen shows

Table 2

Grain size of the matrix phase, area fraction of the second phases and fractal dimension of the maximum connected second phases in all the alloy specimens.

Specimens	Grain size (μm)	Area fraction of second phase (%)	Fractal dimensions
CA0.0	354 ± 43	2.1 ± 0.1	1.11 ± 0.04
CA0.5	305 ± 11	2.8 ± 0.1	1.12 ± 0.07
CA1.5	202 ± 2	4.1 ± 0.1	1.28 ± 0.09
CA2.0	161 ± 5	7.2 ± 1.0	1.62 ± 0.11

sporadically distributed fine second phase particles with solid white contrast, both inside the grains as well as at the grain boundaries in **Fig. 2(a)**. There are two types of shapes noticeable in the phases in **Fig. 2(a)**. Some of the equiaxed shaped particles are indicated by yellow arrows, while one of the few irregular shaped ones is pointed out by green arrow in **Fig. 2(a)**. The equiaxed particles are also visible in the CA0.5 specimen, as pointed out by yellow arrows in **Fig. 2(b)**. There is an additional phase present both inside the grains and at the boundaries in this specimen, which is irregular in shape (pointed out by green arrows in **Fig. 2(b)**). A magnified view of the morphology of this type of phase is shown in **Fig. 2(c)**. This phase appears to have partly solid contrast like a divorced eutectic (pointed out by red arrow in **Fig. 2(c)**) and partly defined lamellar structure (marked by a blue arrow in **Fig. 2(c)**). In CA1.5 specimen, the equiaxed particles are lesser in number (indicated by yellow arrows in **Fig. 2(d)**). There is a new kind of phase visible both inside the grains and at the grain boundaries, as marked by green arrows in **Fig. 2(d)**. The morphology of this phase appears as fine or short lamellar eutectic type, as shown in the magnified image in **Fig. 2(e)**. The presence of similar kind of morphology in the island-like phases inside the grains (as shown by the purple arrow in **Fig. 2(e)**) suggests that this is the same kind of eutectic phase which are present at the boundaries (indicated by orange arrows in the same figure). Further, the overall size, fraction, and connectivity of the second phases appear to be

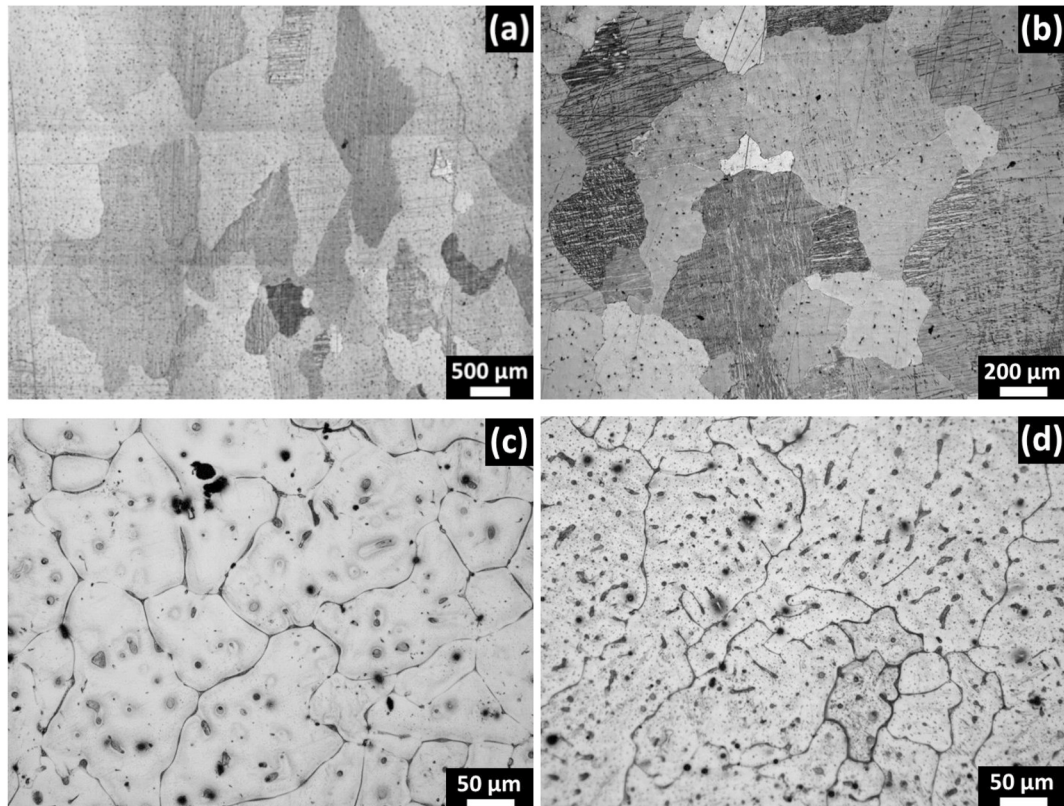


Fig. 1. Optical micrographs of the (a) CA0.0 (stitched), (b) CA0.5, (c) CA1.5, and (d) CA2.0 specimens.

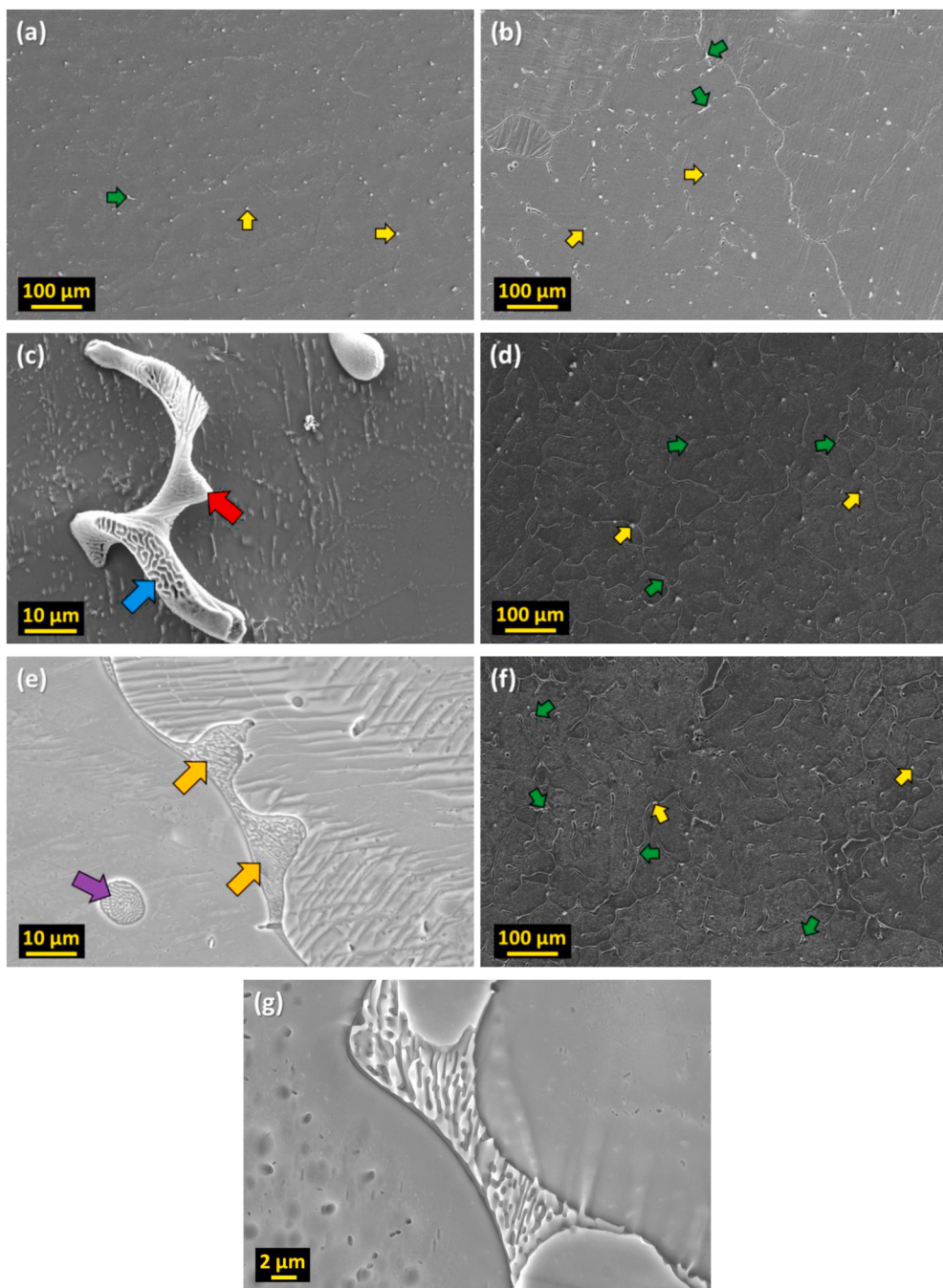


Fig. 2. SEM images showing the distribution of second phases in (a) CA0.0, (b,c) CA0.5, (d,e) CA1.5, and (f,g) CA2.0 specimens.

significantly higher in CA1.5 specimen (Fig. 2(d)) than the previously mentioned specimens. In the CA2.0 specimen, the equiaxed particles inside the grains are fewer in number (indicated by yellow arrows in Fig. 2(f)). The presence of the lamellar eutectic type phase both inside the grains and at the boundaries, as pointed by green arrows in Fig. 2(f), is more prevalent in terms of the fraction as well as connectivity in this specimen. The short lamellar eutectic type morphology of this phase is visible in the magnified image (Fig. 2(g)), thus indicating that the phase is similar to the one shown in CA1.5 specimen (Fig. 2(e)). The combined area fractions of all the second phases were estimated from the SEM images and are presented in Table 2. It can be inferred from Table 2 that the second phase area fraction increases as the Ca concentration, and thereby the Ca/Al ratio, are increased in the alloys.

3.1.3. Connectivity of the second phase networks

Fractal analyses were conducted for studying the variation in the connectivity of the second phase networks as visible in SEM images (Fig. 2(a,b,d,f)). Representative binary images of the maximum connected boundaries in the microstructures of CA0.0, CA0.5, CA1.5, and CA2.0 specimens are presented in Fig. 3(a-d), respectively. As visible in Fig. 3(a), the second phases are sporadically formed in the CA0.0 specimen. Despite having a comparatively larger network, the second phases are still in the form of small isolated clusters in the CA0.5 specimen (Fig. 3(b)). In the CA1.5 specimen (Fig. 3(c)), the second phases have formed much larger networks in comparison to the CA0.0 (Fig. 3(a)) and CA0.5 (Fig. 3(b)) specimens. Finally, the second phases in CA2.0 specimen have formed in large clusters of strongly connected networks (Fig. 3(d)). The connectivity of the second phase networks are

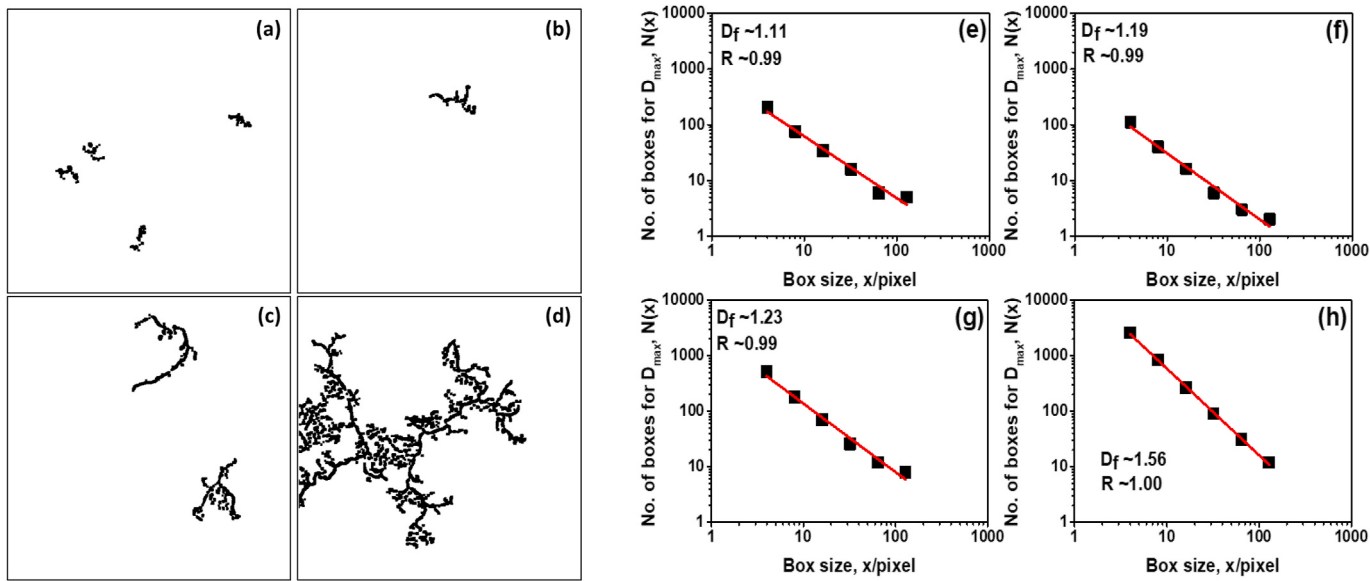


Fig. 3. Fractal analyses showing (a–d) maximum connected grain boundaries extracted from the representative binary SEM images of the microstructures in (a) CA0.0, (b) CA0.5, (c) CA1.5, and (d) CA2.0 specimens; (e–h) fractal dimension (D_f) plots obtained through box counting of the corresponding images in (a–d).

further quantified in terms of fractal dimensions (D_f) for better comparisons (Table 2). For this purpose, the fractal dimension plots in Fig. 3 (e–h) were constructed by employing the ‘box-counting method’ from Fig. 3(a–d), respectively, and the slope of each of these plots was estimated. Evidently, the plot in Fig. 3(e) shows that the slope is lowest for the CA0.0 specimen. It gradually increases in the CA0.5 specimen (Fig. 3(f)) and more so in the CA1.5 specimen (Fig. 3(g)). The slope increases significantly for the CA2.0 specimen in Fig. 3(h). The D_f values presented in Table 2 are the average values of such slopes obtained by analyzing multiple SEM images of similar magnifications for each of the alloy compositions. It should be noted that the value of D_f close to 1 implies that the particles are mostly isolated, whereas a D_f value approaching 2 indicates a well-connected network [33,35]. Hence it can be inferred from the D_f values in Table 2, that the higher Ca content and thereby higher Ca/Al content ratio, lead to stronger connectivity of the second phase network.

3.2. Phase analyses

3.2.1. Evolution of phases

The evolution of phases for the specimens with varying Ca/Al ratio is studied through XRD analysis, as presented in Fig. 4(a). Owing to the presence of the strong peaks of the matrix phase (Mg), the relatively weaker second phase peaks are not visible in Fig. 4(a). In order to identify the peaks from the second phases, the 2θ range of 26° – 46° (as enclosed in the dashed rectangular area in Fig. 4(a)) is further magnified by reducing the intensity ranges in Fig. 4(b). The stacked XRD plots in Fig. 4(b) suggests the presence of Al–Mn and Ca-rich second phases in the Mg matrix phase in all the as-cast alloys. The XRD profile corresponding to the CA0.0 specimen in Fig. 4(b) indicates the presence of Al_8Mn_5 , γ - $\text{Mg}_{17}\text{Al}_{12}$, and C36-(Mg,Al)₂Ca (ternary Laves phase) phases in the microstructure. The γ - $\text{Mg}_{17}\text{Al}_{12}$ phase could not be found in any of the other specimens. The presence of the Al_8Mn_5 phase in the CA0.5, CA1.5, and CA2.0 specimens could be speculated from the corresponding small peaks in the XRD profiles in Fig. 4(b). The XRD profile corresponding to the CA0.5 specimen in Fig. 4(b) suggests that the C36-(Mg,Al)₂Ca phase dominates the microstructure in this composition. A strong presence of the C14-Mg₂Ca phase could be detected in both the CA1.5 specimen and CA2.0 specimens. Apart from these phases, the presence of the C15-Al₂Ca phase is also hinted by the small peaks in the CA0.5 and CA1.5 specimens.

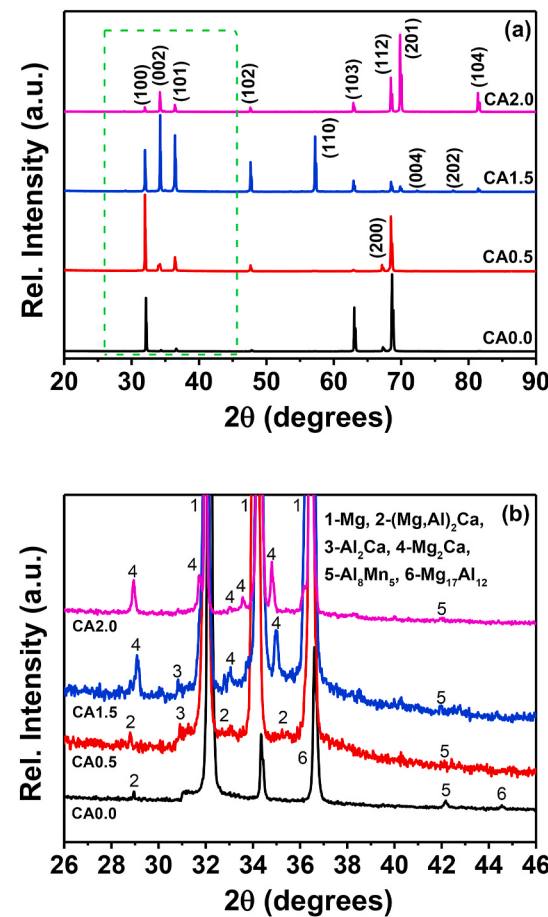


Fig. 4. XRD profiles of all the specimens within the 2θ ranges of (a) 20–90° with only Mg phase indexed, and (b) further magnified within 26–46° to show the second phases along with Mg.

3.2.2. Variation in lattice parameters

The lattice parameters of the matrix phase were estimated using Cohen’s method [27,28] from the broadening of the diffraction peaks in

Fig. 4(a). The variation in both the lattice constants a and c , as well as their ratios (*i.e.* c/a), for the different alloy compositions are shown in **Table 3**. Evidently, the specimen with the lowest Ca/Al content ratio (*i.e.* CA0.0) exhibits the largest lattice constant values. With increasing Ca/Al content in the alloys, lattice parameter values decrease (**Table 3**) as they approach the values corresponding to pure Mg: $a = 0.32092$ nm, $c = 0.52099$ nm (JCPDS 00-004-0770) [27].

3.2.3. Morphology and composition of the second phases

The morphologies and compositions of the second phases observed in different alloys are unveiled through the SEM images and corresponding EDS analyses, respectively, in **Fig. 5**. The faceted particles in the CA0.0 specimen in **Fig. 5(a)** are the ones indicated by yellow arrows in **Fig. 2(a)**. As visible from the EDS analysis in **Fig. 5(b)**, this phase is enriched in Al and Mn. The XRD analysis in **Fig. 4(b)** has confirmed the presence of the Al_8Mn_5 phase in all the specimens (including CA0.0), which suggests that the particles in **Fig. 5(a)** is of the same phase. Similar faceted morphology of this phase has also been reported by Zeng et al. [45,46]. Moreover, the presence of the Al_8Mn_5 phase is also verified through thermodynamic analysis, as discussed later in section 4.1.1. This type of particles is also observed in CA0.5 (in **Fig. 2(b)**), CA1.5 (in **Fig. 2(d)**) and CA2.0 (in **Fig. 2(f)**) specimens (indicated by yellow arrows), as already mentioned in section 3.1.2. The fine elongated phase in the CA0.0 specimen in **Fig. 5(c)**, similar to the one marked with a green arrow in **Fig. 2(a)**, shows the presence of only Mg and Al in the corresponding EDS analysis in **Fig. 5(d)**. Hence, this phase can be confirmed to be the $\text{Mg}_{17}\text{Al}_{12}$ phase. The high Mg content (see **Fig. 5(d)**) must have originated from the large beam diameter in EDS analysis that covers a significant volume of the matrix phase surrounding the fine particles. The eutectic phase in the CA0.5 specimen in **Fig. 5(e)**, similar to the ones shown in **Fig. 2(b and c)**, corresponds to the $\text{C}36-(\text{Mg},\text{Al})_2\text{Ca}$ phase. The corresponding EDS analysis in **Fig. 5(f)** matches with the EDS analyses of the $\text{C}36-(\text{Mg},\text{Al})_2\text{Ca}$ phase in earlier studies [20,44]. Moreover, Li et al. [24] reported both divorced eutectic as well as lamellar eutectic type morphology of this phase, similar to those observed in **Fig. 2(c)**. The short lamellar eutectic type phases predominantly found in CA1.5 (**Fig. 2(e)**) and CA2.0 specimens (**Fig. 2(g)**) are shown in **Fig. 5(g)** and **(i)**, respectively. The EDS analyses corresponding to **Fig. 5(g)** and **(i)** are shown in **Fig. 5(h)** and **(j)**, respectively. Both the EDS analyses in **Fig. 5(h)** and **(j)** exhibit similar compositions, where the Ca content is higher than the Al content. This composition is closer to that of the $\text{C}14-\text{Mg}_2\text{Ca}$ phase reported by Li et al. [24].

In order to confirm the composition of the coarse eutectic second phase in CA2.0 specimen (like the one shown in **Fig. 5(i)**), 3DAP analysis has been carried out (**Fig. 6**). For this analysis, several tips of $\sim 225\text{--}350$ nm length were prepared from the CA2.0 specimen with the help of FIB. The eutectic second phase, along with its interface with the matrix, could be traced in the 3D reconstructed volumes. One such 3D reconstructed volume is shown in **Fig. 6(a)**, where the various elements *viz.* Mg, Al, and Ca are mapped in red, green, and yellow colors, respectively. Two distinct regions can be easily traced in **Fig. 6(a)**, among which the bottom-right region is enriched in Ca. To visualize the interface between these two regions, an iso-concentration surface (with Ca concentration maintained at 10 at.%) [47,48] has been constructed in **Fig. 6(b)**. Several other smaller interfaces are also visible in **Fig. 6(b)**, which are

part of similar Ca-rich phases. A proxigram [48] corresponding to the larger iso-concentration surface (**Fig. 6(b)**) has been plotted in **Fig. 6(c)**. The distance in this figure is in the normal direction to both sides of the interface (shown by arrows in **Fig. 6(b)**), whereas the atomic concentration values are integrated across the total interface area. The atomic concentrations of Mg, Al and Ca in **Fig. 6(c)** lie within the composition range of the $\text{C}14-\text{Mg}_2\text{Ca}$ phase as reported in Ref. [44]. Therefore, this phase can be confirmed as the $\text{C}14-\text{Mg}_2\text{Ca}$ phase with dissolved Al. The presence of a similar ternary $\text{C}14-\text{Mg}_2\text{Ca}$ phase in Mg-Al-Ca-Mn alloys has also been observed by Elamami et al. [22]. The similarity in the composition of the eutectic phases observed in CA1.5 and CA2.0 specimens in **Fig. 5(h)** and **(j)**, respectively, indicates that the lamellar eutectic second phase in CA1.5 specimen (**Fig. 5(g)**) also corresponds to the $\text{C}14-\text{Mg}_2\text{Ca}$ phase.

3.3. Evaluation of mechanical properties

3.3.1. Nano-hardness of individual phases

Nano-indentation tests were conducted for the mechanical characterization of the matrix and the coarse eutectic second phases (**Fig. 7**). The representative indentation load vs. depth profiles presented in **Fig. 7(a)** and **(b)** correspond to the matrix phase and the eutectic second phases, respectively. The eutectic second phase in CA0.0 specimen (*i.e.* the $\text{Mg}_{17}\text{Al}_{12}$ phase) is very fine in size, as visible from **Figs. 2(a)** and **Fig. 5(c)**. Consequently, it becomes extremely difficult to execute indentations which are confined entirely inside these phases, without directly deforming the matrix phase. Hence no curve corresponding to the eutectic second phase in CA0.0 specimen is shown in **Fig. 7(b)**. Some of the indentation marks in both the matrix (indicated by arrows) and the second phase (enclosed in dotted triangles in the image and the enlarged inset image) in the CA2.0 specimen are shown in the SEM images in **Fig. 7(c)**. The average instrumented elastic modulus (E , in GPa) and nano-hardness (in VHN) values corresponding to the matrix phase and the second phases in different alloy compositions are tabulated in **Table 4**. It is observed from **Table 4** that both the nano-hardness and E values of the matrix phase decrease with the rise in the Ca/Al ratio in the compositions. In contrast, the nano-hardness and the elastic modulus corresponding to the second phase increases with increasing Ca/Al content (**Table 4**). The distinctively higher hardness and elastic modulus values of the eutectic second phases highlight its hard and brittle nature in comparison to the softer matrix phase, especially in CA1.5 and CA2.0 specimens (**Table 4**).

3.3.2. Micro-hardness and tensile properties of bulk alloy specimens

The variation in the micro-hardness with the Ca/Al content ratio is illustrated in **Fig. 8(a)**. Clearly, the increase in the Ca/Al content ratio leads to an increase in the hardness values of the alloy specimens. In contrast, the tensile stress-strain curves (**Fig. 8(b)**) for the different as-cast alloy compositions show an exactly opposite trend, with the CA0.0 specimen exhibiting maximum yield strength (YS $\sim 130 \pm 5$ MPa), ultimate tensile strength (UTS $\sim 183 \pm 9$ MPa) and appreciable uniform elongation (UEL $\sim 3.3 \pm 0.2\%$). The CA0.5 specimen achieves better elongation (UEL $\sim 4.8 \pm 1.6\%$) compared to CA0.0 specimen, albeit with much lower strength (YS $\sim 90 \pm 7$ MPa, UTS $\sim 150 \pm 16$ MPa). The YS in CA1.5 specimens is slightly lower ($\sim 84 \pm 10$ MPa), while the elongation ($\sim 1.6 \pm 0.5\%$) and UTS ($\sim 105 \pm 21$ MPa) values are significantly lower than the CA0.5 specimen. Surprisingly, the CA2.0 specimens fail as soon as plastic deformation is initiated and much before reaching the 0.2% offset yield point (refer to the enlarged curve shown in the inset of **Fig. 8(b)**), indicating an extremely poor work hardening response.

In order to assess the work hardening response in the CA0.0, CA0.5, and CA1.5 specimens, the rate of work hardening (normalized by dividing with respective true YS values [49]) is plotted against true strain in **Fig. 8(c)**. Some significant stages of the work hardening curves are also indicated in **Fig. 8(c)**. These stages are distinguished by different

Table 3

Lattice parameters of the matrix phase estimated through XRD analysis using Cohen's method in all the alloy specimens.

Specimens	Lattice Parameters (Å)		c/a ratio
	a	c	
CA0.0	3.43	5.60	1.63
CA0.5	3.36	5.52	1.64
CA1.5	3.25	5.29	1.63
CA2.0	3.12	5.04	1.62

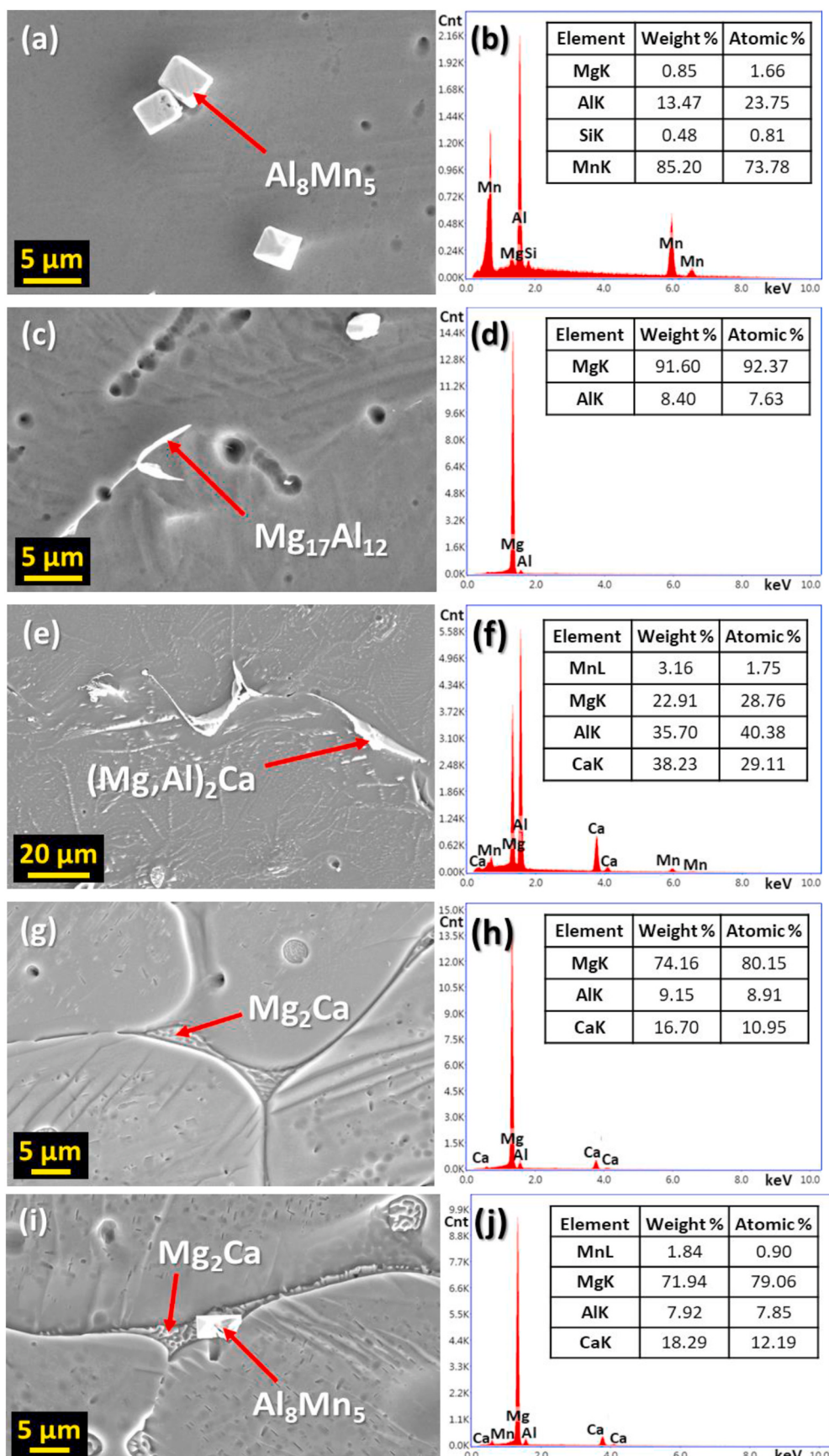


Fig. 5. SEM-EDS analyses showing (a) Al_8Mn_5 phase with corresponding (b) EDS analysis, and (c) $\gamma\text{-Mg}_{17}\text{Al}_{12}$ phase with corresponding (d) EDS analysis in CA0.0 specimen; (e) $(\text{Mg},\text{Al})_2\text{Ca}$ phase with corresponding (f) EDS analysis in CA0.5 specimen; (g) Mg_2Ca phase with corresponding (h) EDS analysis in CA1.5 specimen; and (i) Mg_2Ca phase with corresponding (j) EDS analysis in CA2.0 specimen.

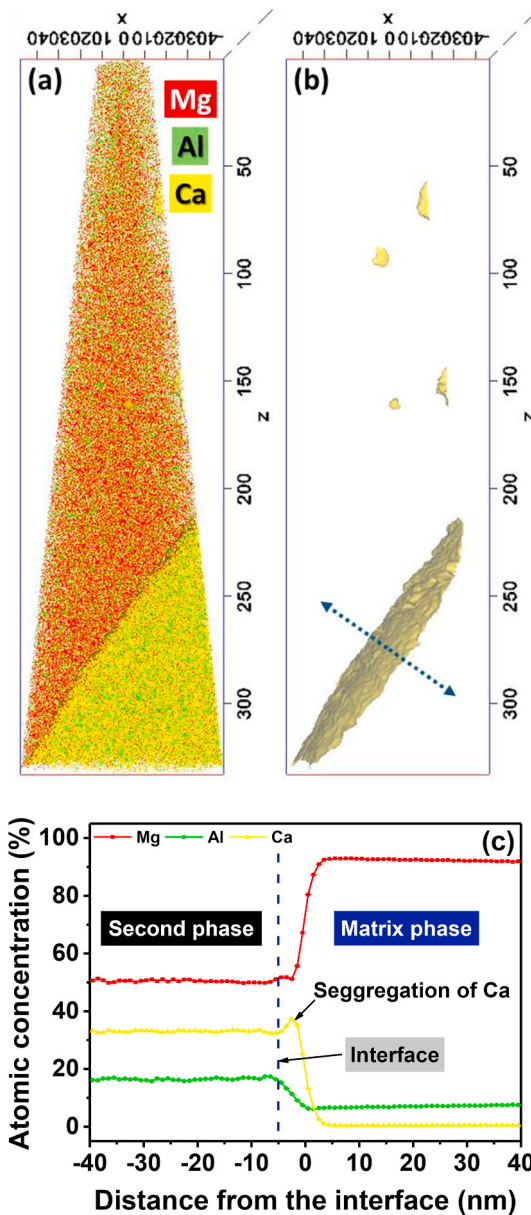


Fig. 6. 3D reconstruction of an atom probe analyzed volume in CA2.0 specimen showing (a) the distribution of Mg, Al and Ca atoms; (b) iso-concentration (10 at.-% Ca) surfaces indicating matrix/second phase interfaces; (c) atomic concentration profile in proximity to both sides of the large interface, as indicated in (b). All dimensions in (a) and (b) are in nm.

dislocation interaction mechanisms. Stage I corresponds to slip in single crystals, while stage II is linear hardening due to the initiation of slip in single crystals as well as poly-crystals [50–52]. In the presence of extended stage III to V, as shown in Fig. 8(c), stage I and II become insignificant and hence, not shown in the figure. The work hardening rates corresponding to the rest of the stages are estimated from the slopes of the curves in Fig. 8(c) and are tabulated in Table 5. The negative signs for all the entries in this table indicate that the work hardening rate shows an overall decreasing trend in all the alloys, once yielding initiates. However, the magnitude of these slopes varies between stages and alloy compositions, thus highlighting the varied work hardening responses of the alloys. The slopes of stage III are represented by two values (denoted as 1 and 2 in Table 5) since all the curves exhibit a substantial amount of slope change at this stage. Stage III is known as a recovery stage that follows the linear hardening stage due to the activation of different slip systems in different grains [50–52]. The

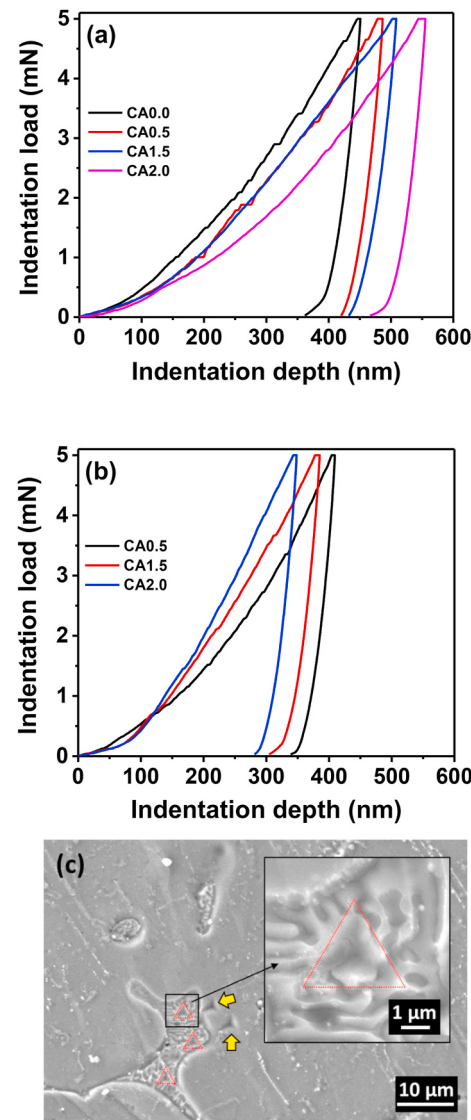


Fig. 7. Nano-indentation test results showing the indentation load vs. depth profiles (a) in the matrix phase and (b) in the second phases in all the alloy specimens. Some of the indentation marks on the matrix and the second phase in CA2.0 specimen has been shown in (c).

Table 4

Instrumented elastic modulus (E) and nano-hardness (H) values of the matrix phase and the eutectic second phase.

Specimens	Matrix phase		Eutectic second phase	
	E (GPa)	H (VHN)	E (GPa)	H (VHN)
CA0.0	47.1 ± 4.3	80.4 ± 9.8	–	–
CA0.5	44.8 ± 4.2	66.6 ± 8.4	62.3 ± 2.8	105.0 ± 7.2
CA1.5	43.1 ± 2.0	65.7 ± 8.8	67.6 ± 5.1	129.9 ± 20.8
CA2.0	42.4 ± 8.8	46.2 ± 5.7	67.8 ± 2.5	138.1 ± 9.4

increased activity of dislocations through activation of different slip systems during stage III leads to increased dislocation interactions and thereby, to increased hardening at stage IV. Stage V is the final dynamic recovery stage that is dominated by softening and ultimately leads to necking and failure [52]. The stage III, IV and V slopes are significantly low in both CA0.0 and CA0.5 specimens in comparison to CA1.5 specimen (Table 5). This indicates that the CA0.0 and CA0.5 specimens exhibit better hardening response than the CA1.5 specimen. It is to be

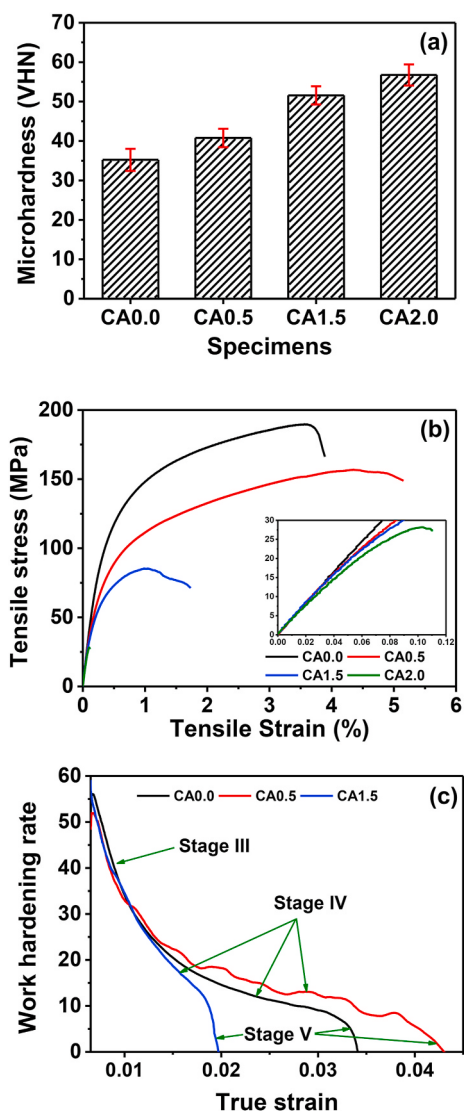


Fig. 8. Mechanical behavior of the as-cast alloy specimens showing (a) variation in microhardness values for all the compositions, (b) tensile stress-strain curves for all the compositions (inset: magnified view of the curve corresponding to CA2.0 specimen), and (c) normalized rate of work hardening (vs. true strain) curves for CA0.0, CA0.5 and CA1.5 specimens.

Table 5

Slopes at different stages of the work hardening curves in CA0.0, CA0.5 and CA1.5 specimens.

Specimens	Stage III		Stage IV	Stage V
	(1)	(2)		
CA0.0	-6465.8	-2340.0	-648.6	-5497.9
CA0.5	-6141.1	-2293.6	-552.3	-1621.2
CA1.5	-7846.4	-4374.3	-2308.6	-11512.8

noted that the CA0.5 specimen shows comparatively lower slopes than the CA0.0 specimen in all the stages of work hardening (Table 5). This indicates that the former specimen shows better work hardening response and thereby, delays the onset of failure mechanisms.

3.4. Fracture behavior

The fracture behavior of all the alloy specimens was analyzed by studying the fractured surfaces as well as the propagation of cracks

through the microstructure along the tensile direction, as presented in Fig. 9(a-f), Fig. 10(a-d) and Fig. 11(a-d). The propagation of cracks is studied from SEM images of tensile tested specimens captured from the surfaces perpendicular to the fractured surfaces (i.e. along the tensile loading direction), as schematically shown in Fig. 9(f). The fracture surface in the CA0.0 (Fig. 9(a)) specimen shows numerous ridges (indicated by blue arrows) and cleavages (indicated by yellow arrows) suggesting a brittle mode of fracture. However, there are few visible micro-voids (marked by red arrows in Fig. 9(a)) that reveal the partially ductile nature of fracture surface in this specimen. As visible from Fig. 9(b), cracks in the CA0.0 specimen have formed and propagated along a path that does not coincide with the grain boundaries or second phase interfaces. The fracture surface of the CA0.5 alloy specimen (Fig. 9(c)) also shows predominantly brittle mode of fracture, as indicated by the various ridges (blue arrows) and cleavages (yellow arrow). However, the presence of few micro-voids (marked by red arrow in Fig. 9(c)) indicates the partially ductile nature of the fracture surface in this specimen, akin to the CA0.0 specimen. In the CA0.5 alloy specimen, cracks can be found both at the interfaces of the matrix/second phases (Fig. 9(d)) as well as inside the grains (Fig. 9(e)). The CA1.5 specimen have undergone completely brittle fracture as suggested by the ridges (indicated by blue arrows) and cleavages (indicated by yellow arrows) visible in Fig. 10(a). The cracks have propagated primarily along the network of the eutectic second phases in this specimen, as shown in Fig. 10(b). The magnified views presented in Fig. 10(c-d), corresponding to the regions marked in Fig. 10(b), suggest that both fragmentation of the eutectic second phase (Fig. 10(c)) and decohesion between the matrix and the second phase (Fig. 10(d)) contributed to crack formation in this specimen. The fracture surface in CA2.0 specimen also reveals ridges (indicated by blue arrows) and cleavages (indicated by yellow arrows) in Fig. 11(a), suggesting it has also undergone complete brittle type of fracture. Similar to the CA1.5 specimen, the cracks have propagated along the eutectic second phase network in CA2.0 specimen (Fig. 11(b)). Decohesion between the matrix and the second phase (Fig. 11(c-d)) as well as fragmentation of the second phase (Fig. 11(d)) can also be observed in the regions magnified from Fig. 11(b). Additionally, some fine cracks have propagated inside the matrix from the interface in this specimen (Fig. 11(c)).

4. Discussion

4.1. Effect of Ca/Al ratio on microstructural evolution

4.1.1. Effect of Ca/Al ratio on second phase evolution

The XRD analysis (Fig. 4), SEM analysis (Fig. 5) and 3DAP analysis (Fig. 6) reveal the formation of different coarse Ca-rich eutectic phases in the as-cast Mg-Al-Ca-Mn alloys. The fraction of second phases formed at the end of solidification are estimated through thermodynamic calculations using Scheil cooling conditions and the results are presented in Fig. 12. The Al₈Mn₅ phase is present in all the specimens as predicted from the thermodynamic calculations (Fig. 12(a)) as well as observed from the XRD results (Fig. 4(b)). The small fractions of this phase in all the specimens (Fig. 12(a)) justify the corresponding small peaks in the XRD profiles (Fig. 4(b)). This phase is present in all the specimens (Fig. 2(a,b,d,f)), primarily in the form of fine equiaxed faceted particles, as shown in Fig. 5(a), as also previously observed in literature [24,26,45,53]. The Al₈Mn₅ content in the CA0.5 specimen is very low (~0.01% in Fig. 12(a)) due to the low Mn content in the alloy composition (Table 1). Presence of the C15-Al₂Ca phase could not be detected through microscopy in any of the specimens, despite it being detected during XRD analysis in CA0.5 and CA1.5 specimens (Fig. 4(b)). This suggests that this phase may have formed in negligible fraction due to favourable local composition during solidification. Nevertheless, this phase is not expected to form during solidification [19,54].

Presence of the eutectic γ -Mg₁₇Al₁₂ phase is detected in the form of fine particles in CA0.0 specimen (Figs. 4(b), 2(a) and 5(c and d)), where

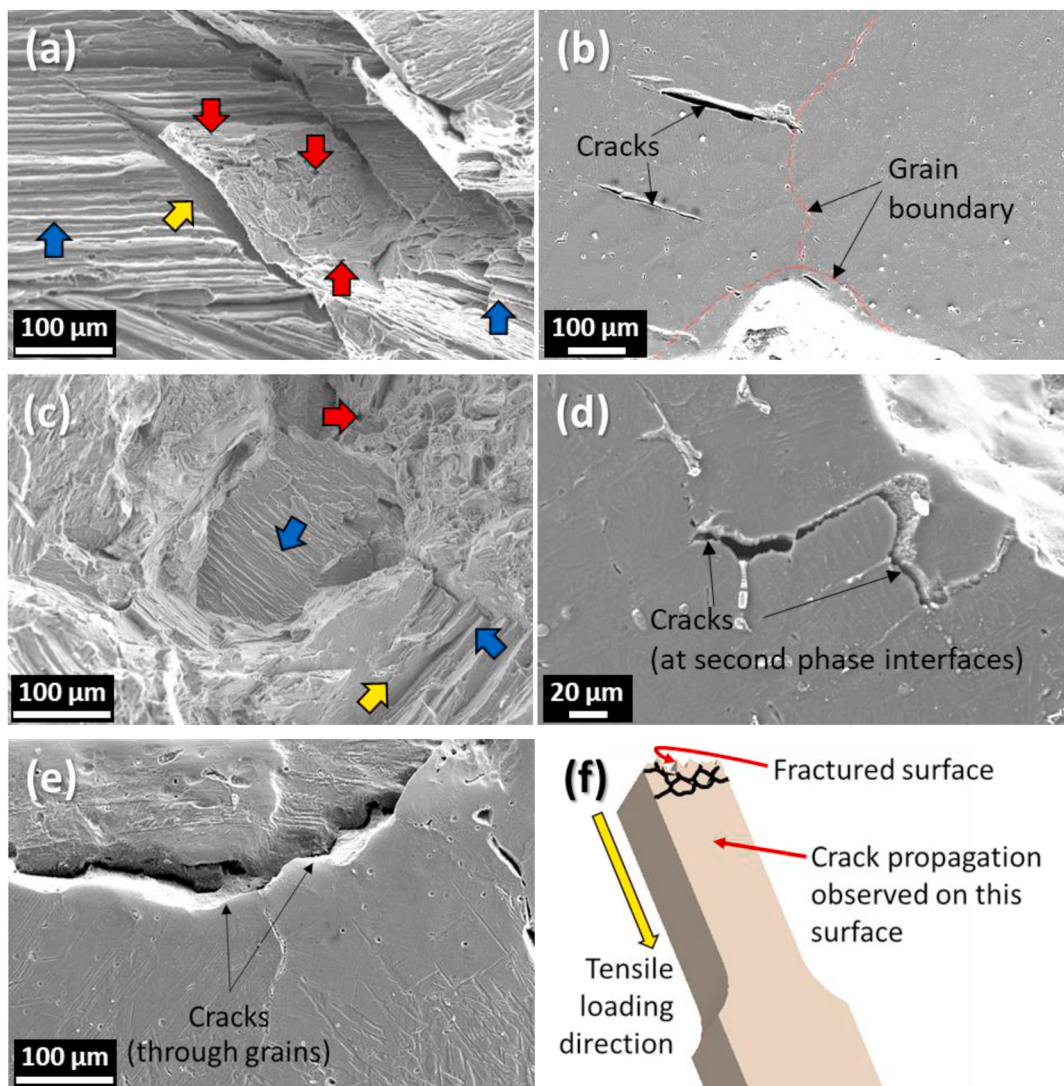


Fig. 9. Fracture behavior study of the (a,b) CA0.0 and (c–e) CA0.5 specimens showing (a,c) the fractured surfaces and (b,d,e) propagation of cracks on the surface parallel to the tensile loading direction, as schematically shown in (f).

both the Ca concentration and the Ca/Al ratio are low (Table 1). The thermodynamic calculations in Fig. 12(a) also suggest its presence in the same specimen. Kondori et al. [10] have also reported the presence of this phase in an Mg alloy with low Ca/Al ratio (~ 0.08), even at higher Ca content (0.5 wt%). Hence, it can be inferred that the Ca/Al ratio, and not the Ca content, dictates the formation of the $Mg_{17}Al_{12}$ phase in Mg-Al-Ca-Mn alloys. In contrast to the thermodynamic calculations (Fig. 12(a)) as well as the XRD analysis (Fig. 4(b)), presence of the C36-(Mg,Al)₂Ca phase is not detected in CA0.0 specimen during SEM analysis. This implies that the evolution of this phase during solidification of the low Ca-containing CA0.0 alloy (Table 1) may have been restricted to a few locations depending on the local composition. On the contrary, the C36-(Mg,Al)₂Ca phase is prevalent in CA0.5 specimen (Figs. 4(b), Fig. 2(b,c), Fig. 5(e and f)), where both the Ca concentration and the Ca/Al ratio are increased as compared to the CA0.0 specimen. The thermodynamic calculations in Fig. 12(a) also predicts the dominating presence of this phase in CA0.5 specimen. On the other hand, the thermodynamic calculations (Fig. 12(a)) suggest the formation of the C14-Mg₂Ca phase in both the CA1.5 and CA2.0 specimens, as also supported by the XRD analysis (Fig. 4(b)). The SEM analyses reveal the short lamellar eutectic type morphology of this phase in both CA1.5 (Figs. 2(e) and Fig. 5(g)) and CA2.0 (Figs. 2(g) and Fig. 5(i)) specimens. The composition of this phase is further verified by the 3DAP analysis in

Fig. 6(c). The high fractions of this eutectic phase in CA1.5 and CA2.0 specimens, as predicted in Fig. 12(a), can be visually confirmed from the SEM images in Fig. 2(d) and (f), respectively.

The variations in the nano-hardness values of the eutectic second phases in CA0.5, CA1.5, and CA2.0 specimens (Table 4) can be accredited to the different variants of the eutectic phases, viz. (Mg, Al)₂Ca and Mg₂Ca, in the respective microstructures. The lower nano-hardness value (~ 105 VHN) of the second phase in the CA0.5 specimen (see Table 4) can be correlated to the C36-(Mg,Al)₂Ca phase present in this specimen. On the other hand, the C14-Mg₂Ca phases present in the CA1.5 and CA2.0 specimens show higher hardness values (~ 130 -138 VHN), as shown in Table 4.

4.1.2. Effect of Ca content and Ca/Al ratio on the second phase fraction and connectivity

The overall area fraction of the second phases increases with the Ca content and Ca/Al ratio as shown in Table 2. Although the phase fraction values from the thermodynamic calculations (Fig. 12(a)) appear to be slightly lower than that obtained through SEM image analyses (Table 2), the trends shown in both of them are the same for all the alloy specimens. The fractal dimensions measured from Fig. 3 and summarized in Table 2, reflect the higher connectivity of the second phase networks at higher Ca/Al content ratio of the alloy compositions. It appears that both

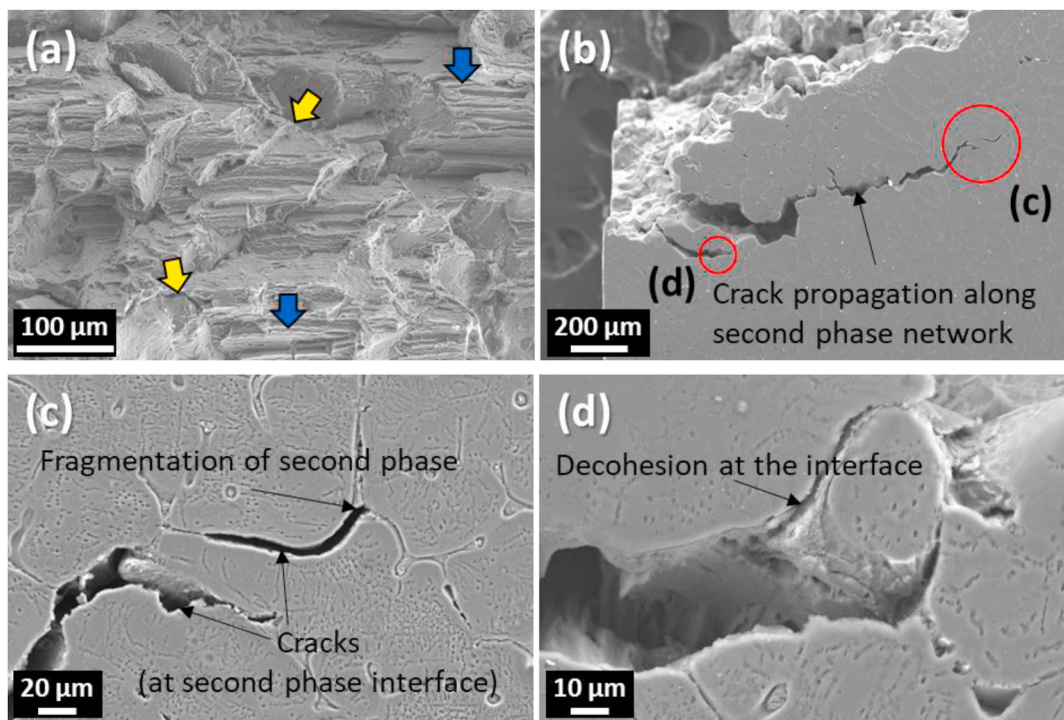


Fig. 10. Fracture behavior study of the CA1.5 specimen showing (a) the fractured surface and (b-d) propagation of cracks on the surface parallel to the tensile loading direction, as schematically shown in Fig. 9(f). The images in (c) and (d) are magnified views of the regions indicated in (b).

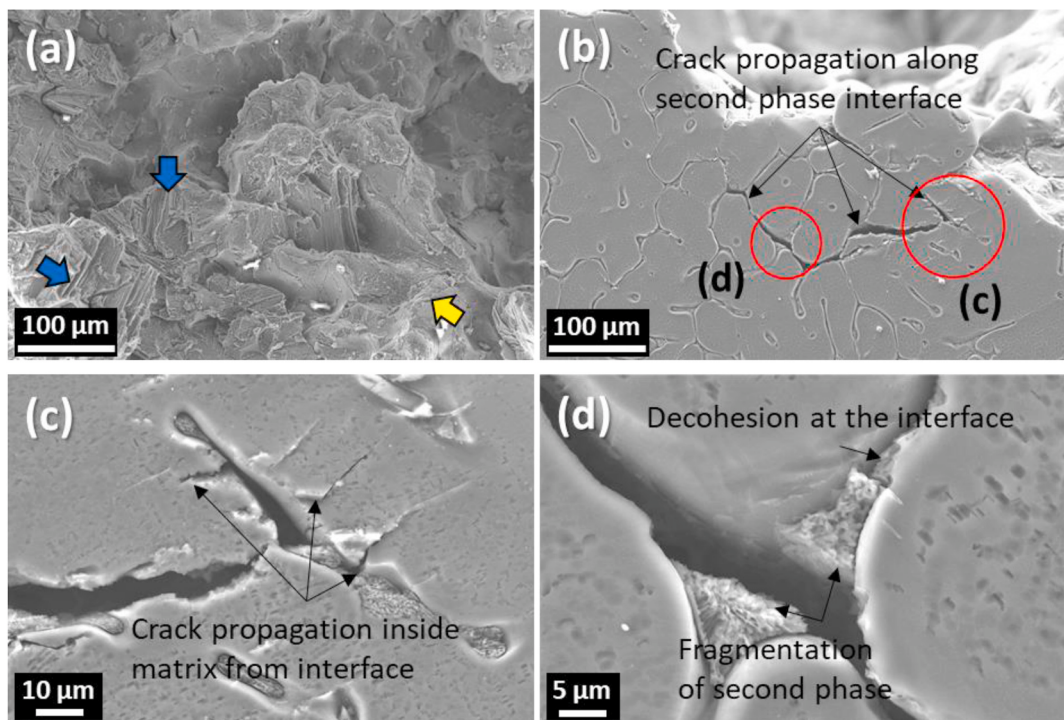


Fig. 11. Fracture behavior study of the CA2.0 specimen showing (a) the fractured surface and (b-d) propagation of cracks on the surface parallel to the tensile loading direction, as schematically shown in Fig. 9(f). The images in (c) and (d) are magnified views of the regions indicated in (b).

the fraction and the connectivity of the second phases are closely related to the Ca concentration and thereby, to the Ca/Al ratio in the alloy composition (Table 1). Some studies attributed the increase in second phase fraction in Mg-Al-Ca-Mn alloys to the increment in the individual [20,24] or overall content of alloying elements [12], despite a decreasing or constant Ca/Al ratio. However, some studies found the

increasing Ca/Al ratio to be the deciding factor for enhancement of the second phase fraction when the total amount of all the alloying elements is more or less constant [25,26]. In this context, Elamami et al. [22] commented that the second phase fraction is independent of the Ca/Al ratio and is a function of type, density, and morphology of the intermetallic phases. However, their observations require further

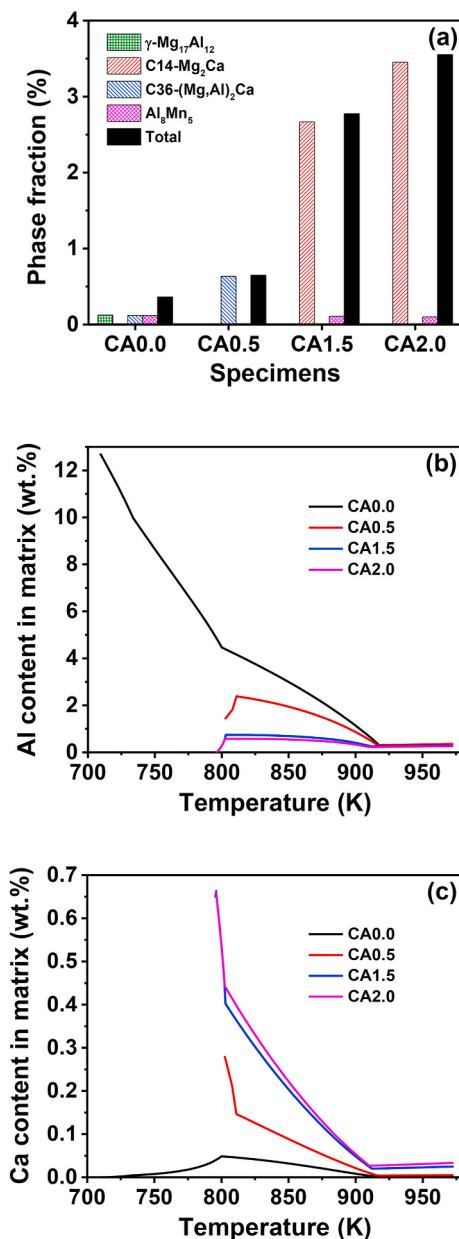


Fig. 12. Thermodynamic calculations of the solidification behavior in all the alloy compositions showing (a) the variation in phase fractions after solidification, and (b,c) the variations in solubility of (b) Al and (c) Ca in the hcp matrix phase with temperature.

verification, considering the narrow range of the Ca/Al ratio (0.58–0.91) studied in the work. Based on the observations from the present investigation, it can be stated that the concentration of alloying elements (in this case, Ca) as well as the Ca/Al content ratio influences the area fraction and connectivity of the second phases, through dictating their type, composition and morphology.

4.1.3. Effect of solute content on the lattice parameters, elastic modulus and the grain size in the matrix phase

The lattice parameters (a and c) as well as the elastic modulus of the matrix phase decrease with the increase in Ca/Al content ratio, as shown in Tables 3 and 4, respectively. The implications of the varying Ca/Al ratio on the lattice parameters and elastic modulus of the hcp Mg matrix phase can be explained with the aid of thermodynamic modeling of the solubility of different elements in the concerned phase. The variations in the solubility of the two major alloying elements viz. Al and Ca in the

hcp Mg phase with temperature, are estimated from the thermodynamic calculations based on Scheil cooling conditions and presented in Fig. 12 (b) and (c), respectively. Considering the high cooling rate maintained during air-cooling of the cast ingots, it can be expected that the solute concentrations in the studied specimens after complete solidification will be very close to those obtained at the respective eutectic temperatures under Scheil cooling conditions. As seen, the solubility of Al in hcp Mg (Fig. 12(b)) is highest in the case of CA0.0 where it increases up to 12.7 wt% at the final eutectic temperature. In the case of CA0.5, the solubility of Al increases up to 2.38 wt% at ~811 K and then decreases to 1.42 wt% at the final solidification temperature. This is due to the formation of the ternary C36-(Mg,Al)₂Ca phase at ~811 K. Understandably, Al partitions in the second phases lead to an overall decrease of Al solubility in hcp Mg. Exactly similar trends are seen in CA1.5 and CA2.0 specimens. On the contrary, the solubility of Ca in the hcp Mg (Fig. 12 (c)) follows exactly the opposite trend as far as the variation in different specimens is concerned. It is highest in CA2.0 and increases up to 0.66 wt% at the final eutectic temperature of 796 K. The Ca solubility in CA1.5 specimen initially lies below that of CA2.0 until it reaches the maximum of 0.66 wt% at 796 K, akin to CA2.0. The steep rise in the Ca concentration at ~803 K in both CA1.5 and CA2.0 specimens is due to the formation of the eutectic hcp Mg phase as a product of the eutectic reaction involving the C14- Mg_2Ca phase. A similar trend is followed in CA0.5 specimen due to the formation of the ternary C36-(Mg,Al)₂Ca phase, although the corresponding temperature (~811 K) as well as the maximum solubility of Ca in hcp Mg is understandably different. The solubility of Ca in the CA0.0 specimen increases up to 0.05 wt% at the eutectic temperature of ~800 K, after which it decreases to almost zero. Evidently, the solubility of Ca in the matrix phase is directly dependent on the concentration of Ca in the alloy composition.

The overall higher solute contents (especially Al) lead to the increments in the lattice parameters (Table 3), elastic modulus (Table 4) and nano-hardness (Table 4) of the hcp matrix phase in alloys with lower Ca/Al content ratio. In addition to the lattice parameters, the grain size of the matrix phase is also significantly influenced by the alloy composition (Table 2). The inverse correlation between the second phase fraction (Table 2 and Fig. 12(a)) and the grain size of the matrix phase (Table 2) indicates that the formation of second phase networks restricts the grain growth during solidification and hence, reduces the grain size in compositions with higher Ca (and Ca/Al) content ratio.

4.2. Correlation between the microstructural evolution and mechanical properties

4.2.1. Influence of microstructural evolution on microhardness

As the grain size of the alloy specimens decreases from ~354 μm to ~161 μm (Table 2) and the coarse second phase fraction increases from 2.1% to 7.2% (Table 2), the microhardness increases from 35 VHN to 57 VHN in the CA0.0 to CA2.0 specimen (Fig. 8(a)). The application of an external force through the indenter instigates localized generation of geometrically necessary dislocations (GNDs) in the material [55,56]. The presence of grain boundaries or second phase interfaces can result in pile-up of those dislocations which restricts further deformation and thereby, increases the hardness of the material. The strengthening from grain boundaries can be expressed using Hall-Petch relationship as [57–60],

$$\sigma_y = \sigma_0 + kD^{-1/2} \quad (2)$$

where σ_0 is the lattice friction stress that can be interpreted as the total contribution from other strengthening mechanisms *viz.* Peierls-Nabarro stress, solid solution strengthening, work hardening, etc. [60], k is the locking parameter and D is the grain size or the distance between the two interfaces. The contribution from the grain size to strengthening (i.e. $kD^{-1/2}$, from Eq. (2)) in each specimen has been estimated by taking $k \sim 0.22 \text{ MPa}\cdot\text{m}^{1/2}$ (for pure Mg [61]). It is minimum for the CA0.0

specimen (~ 12 MPa) and increases gradually with the Ca/Al ratio (~ 13 MPa in CA0.5, ~ 15 MPa in CA1.5 and ~ 17 MPa in CA2.0 specimen). Clearly, the grain boundary strengthening contribution in the alloy and therefore, the resistance of the alloy to indentation i.e. hardness, increase (Fig. 8(a)) with the decrease in grain size (Table 2) with increasing Ca/Al ratio.

Evidently, the second phase fraction or the grain size does not influence the nano-hardness of the matrix, as it decreases from 80.4 VHN to 46.2 VHN with the increment in Ca/Al ratio from 0.06 to 2.21 (Table 4). This can be attributed to the fact that the interactions between the dislocations are confined to localized regions owing to the application of such low load during nano-indentation (~ 8 mN, as compared to ~ 1000 mN of micro-indentation). Instead, the nano-hardness values of the matrix phase (Table 4) have a strong correlation with the variation in lattice parameters (Table 3), which emphasizes the role of solid solution strengthening.

4.2.2. Influence of microstructure and phase evolution on strength

The tensile properties mentioned in section 3.3.2 (Fig. 8(b)), unlike microhardness, deteriorate with an increase in the Ca/Al ratio in the alloy compositions. This suggests that grain refinement is not the dominating strengthening mechanism in the studied alloys, possibly because of the considerably large values of grain size. Such variation in strength can be attributed to the variation in concentration of the solute atoms, *viz.* Al (Fig. 12(b) and Ca (Fig. 12(c)), in the matrix phase. The change in the solute concentration induces variations in the lattice parameters (Table 3) as well as the elastic modulus (Table 4) of the matrix phase. Thus, enhancement in shear YS (τ_{ss}) due to the concentration of substitutional solute atoms (C) is primarily governed by the lattice size effect and the shear modulus effect as follows [62–64],

$$\tau_{ss} = \frac{Ge_s^{3/2} C^{1/2}}{700} \quad (3)$$

where G is the shear modulus of the solid solution or the matrix phase, and the term e_s represents the combined influence of the lattice size and modulus effect. The term e_s in Eq. (3) can be further expressed as,

$$e_s = |\epsilon'_G - \beta \epsilon_b| \quad (4)$$

where $\epsilon'_G = \frac{\epsilon_G}{\left(1 + \frac{|\epsilon_G|}{2}\right)}$, with $\epsilon_G = \frac{1}{G} \frac{dG}{dc} = \frac{1}{E} \frac{dE}{dc}$ being the fractional change in

shear modulus per unit solute concentration, and $\epsilon_b = \frac{1}{a} \frac{da}{dc}$ is the fractional change in the lattice parameter per unit solute concentration. The constant β is usually taken as ~ 3 [62]. The lattice parameters and the elastic modulus values corresponding to the matrix phase from Tables 3 and 4, respectively, are used in both Eq. (3) and Eq. (4) to estimate the contribution of solid solution strengthening to the shear YS of the studied specimens. The term da/dc is calculated only for the lattice parameter a since only basal slip is expected at room temperature in these alloys. The G values were estimated from the measured E values in Table 4, with the help of the following relation,

$$E = 2G(1 - \nu) \quad (5)$$

where ν is the Poisson's ratio ($\nu = 0.29$ for Mg). The increment in tensile YS from solid solution strengthening (σ_{ss}) can be obtained from the tensile shear strength as [60]:

$$\sigma_{ss} = M_{avg} \cdot \tau_{ss} \quad (6)$$

where, M_{avg} is the average Taylor factor. The M_{avg} value can be taken as ~ 4.2 assuming random texture in the as-cast Mg alloys [65]. Therefore, the total YS originated from grain refinement and solid solution can be summarized as [60,66],

$$\sigma_{ys} = (\sigma_u + \sigma_{ss}) + kD^{-1/2} \quad (7)$$

where, σ_u is the YS of pure Mg (~ 24 MPa) at room temperature [67]. The contribution from solid solution strengthening (estimated using Eqs. (3)–(6)) is relatively larger in the CA0.0 specimen (~ 62 MPa), in comparison to the other specimens (~ 55 MPa in CA0.5, ~ 55 MPa in CA1.5 and ~ 54 MPa in CA2.0 specimens). Therefore, the total estimated YS considering grain boundary strengthening, solid solution strengthening and the room temperature YS of pure Mg (using Eqs. (2)–(7)) is ~ 98 MPa for the CA0.0, ~ 92 MPa for CA0.5, ~ 94 MPa for CA1.5, and ~ 95 MPa for CA2.0 specimens.

Although the experimental and estimated YS values for the CA0.5 and CA1.5 specimens are close, the exceptionally higher experimental value than the estimated value of YS in the CA0.0 specimen can be attributed to the fine γ -Mg₁₇Al₁₂ particles shown in Fig. 13. The bright field (BF) and dark field (DF) images in Fig. 13(a) and (b), respectively, depict the interactions between the dislocations and the fine particles in the CA0.0 specimen. The EDS spectrum in Fig. 13(c) (from the particles shown by arrows in Fig. 13(a)) confirms this phase to be the γ -Mg₁₇Al₁₂ phase. These fine particles contribute to YS due to the difference in shear modulus as follows [68],

$$\Delta\sigma_{ys} = \frac{\Delta G}{2\pi^2} \left[\frac{3|\Delta G|}{Gb} \right]^{1/2} \left[0.8 - 0.143 \ln \left(\frac{r}{b} \right) \right]^{3/2} r^{1/2} f^{1/2} \quad (8)$$

where, ΔG is the difference in shear modulus between the matrix and the particles, b is the Burgers vector of the matrix, r is the average radius and f is the fraction of the particles. The shear modulus of the Mg₁₇Al₁₂ phase is taken as 29.14 GPa [69]. The average radius (~ 15 nm) of these particles is estimated from TEM images and the fraction ($\sim 0.12\%$) is obtained from the thermodynamic calculations. The contribution to YS from these nano-sized particles is found to be ~ 22 MPa. Hence, the total estimated YS of the CA0.0 specimen, considering the contributions from solid solution strengthening, grain boundary strengthening and precipitation strengthening is ~ 120 MPa, is much closer to the experimental value of $\sim 130 \pm 2$ MPa. It is to be noted that such precipitation strengthening is not taken into account in any of the other alloy specimens due to the absence of fine γ -Mg₁₇Al₁₂ phase (Figs. 4 and 12(a)).

As mentioned earlier, the estimated YS values considering grain boundary strengthening and solid solution strengthening are ~ 94 MPa and ~ 92 MPa for CA1.5 and CA0.5 specimens, respectively. Although these values are very close to the measured values mentioned in section 3.3.2, the estimated YS is slightly higher in CA1.5 than in CA0.5 specimen, unlike the measured values (~ 84 MPa and ~ 90 MPa, respectively). This can be attributed to the formation of C14-Mg₂Ca phase in the former specimen. The larger differences in the elastic modulus and nano-hardness values between the matrix and the second phase (Table 4) suggest that the interfaces are highly strained in the alloy compositions with higher Ca/Al content ratio. This can be an inherent property of the C14-Mg₂Ca phase, predominantly found in the CA1.5 (Fig. 5(g and h)) and CA2.0 (Fig. 5(i and j)) specimens. Additionally, Fig. 6(c) suggests segregation of Ca atoms (indicated by arrow) near the matrix/second phase interfaces in the CA2.0 specimen. Segregation of large Ca atoms ($\sim 23\%$ larger than Mg atoms) can also be a possible reason behind the highly strained interfaces. Such stress concentration at the interface promotes activation of dislocations sources in multiple grains and thereby, reduce the parameter k in Eq. (2). This, in turn, reduces the experimentally observed YS in CA1.5 specimen (~ 84 MPa) in comparison to the CA0.5 specimen (~ 90 MPa). The estimated YS in CA2.0 specimen is as high as ~ 95 MPa. However, the stress-strain curve corresponding to this specimen in Fig. 8(b) (inset) shows failure at much lower stress, even before reaching the 0.2% strain offset point. The reason behind this is discussed in section 4.2.3.

4.2.3. Correlation between the second phase evolution, area fraction and connectivity with ductility and work hardening

The variations in the ductility (Fig. 8(b)) can be correlated to the second phase distribution (Table 2) in the alloy specimens. As depicted

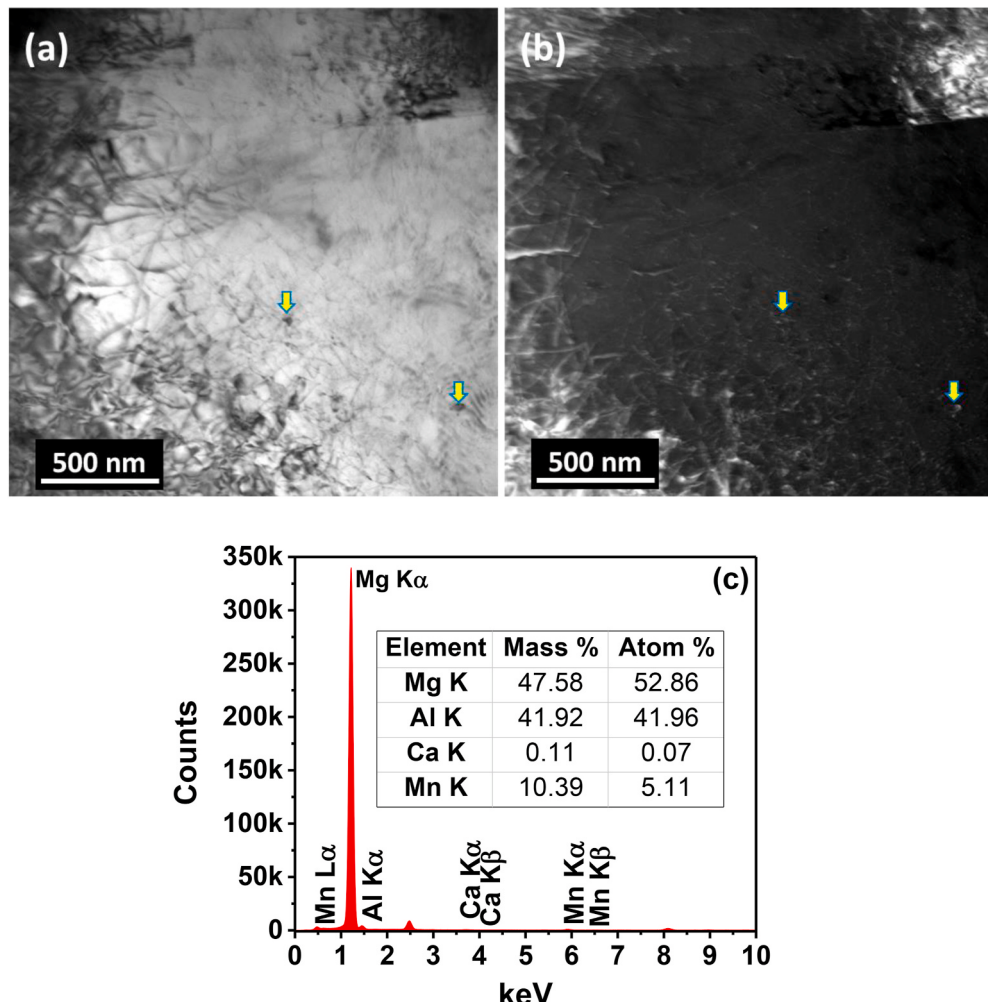


Fig. 13. HRTEM analysis showing (a) bright field images and (b) dark field images of precipitate-dislocation interactions, and (c) EDS analysis from one of the precipitates in the tensile tested CA0.0 specimen.

in Figs. 9(d), Fig. 10(b-d) and Fig. 11(b-d), the second phase networks facilitate the initiation and propagation of cracks during tensile loading. Hence, the strong networks of second phases in CA1.5 and CA2.0 specimens facilitate easy propagation of cracks (shown in Figs. 10(b) and Fig. 11(b), respectively) and lead to poor ductility of in these specimens. Moreover, the eutectic C14–Mg₂Ca phase having larger differences in hardness and elastic modulus with the matrix (Table 4) and with Ca atoms segregated at the interface (Fig. 6(c)), introduce large strains at the interface and thereby, promote decohesion in CA1.5 (Fig. 10(d)) and CA2.0 (Fig. 11(d)) specimens. The eutectic C14–Mg₂Ca phase in the CA1.5 and CA2.0 specimens are also observed to have fragmented in Figs. 10(c) and Fig. 11(d), respectively. This suggests that the C14–Mg₂Ca phase is also brittle in nature. As a result of the larger fraction (Fig. 12(a) and Table 2) and strong connectivity of the brittle C14–Mg₂Ca phase ($D_f \sim 1.66$ in Fig. 3(d,h) and Table 2), the stress required to initiate cracks is attained much before the stress required to activate large scale dislocation movements in the CA2.0 specimen. Consequently, the CA2.0 specimen fails even before reaching the 0.2% strain offset point (Fig. 8(b)) and hence, does not achieve the estimated YS of ~ 95 MPa as mentioned in section 4.2.2. Similarly the CA1.5 specimen also shows poor work hardening response (Fig. 8(c) and Table 5) due to the presence of the C14–Mg₂Ca phase. On the other hand, due to the evolution of other phases, viz. γ -Mg₁₇Al₁₂ (in CA0.0 specimen) and C36-(Mg,Al)₂Ca (in CA0.5 specimen) instead of the C14–Mg₂Ca phase (Figs. 4, 5 and 12(a)), as well as the overall smaller fraction and disconnected networks of the second phase (Fig. 3 and

Table 2), the formation and propagation of cracks are restricted in CA0.0 and CA0.5 specimens (shown in Fig. 9(b) and (d,e), respectively). Hence, these specimens exhibit much better ductility (Fig. 8(b)) and work hardening response (Fig. 8(c) and Table 5). Interestingly, the work hardening response and thereby, the ductility are comparatively better (Fig. 8(b and c) and Table 5) in CA0.5 specimen than in CA0.0 specimen. Considering the similar overall second phase fraction and fractal dimensions (Table 2), this can only be attributed to the evolution of the C36-(Mg,Al)₂Ca phase as the prime eutectic phase in CA0.5 specimen (Fig. 2(b and c), Figs. 4 and 5(e and f) and Fig. 12(a)). The C36-(Mg, Al)₂Ca phase is possibly less detrimental to ductility as compared to the other eutectic phases viz. γ -Mg₁₇Al₁₂ and C14–Mg₂Ca, that dominate the microstructures in the other specimens (Figs. 4, 5 and 12(a)). Both of the γ -Mg₁₇Al₁₂ and the C14–Mg₂Ca phases are known to be detrimental to ductility in Mg alloys [70]. Hence, the UEL is better in CA0.5 specimen ($\sim 4.8\%$) in comparison to all the other specimens. However, in spite of the lesser work hardening response (Fig. 8(c)), the UTS is considerably higher in the CA0.0 specimen than CA0.5 specimen, owing to the much higher YS in the former (Fig. 8(b)). On the other hand, the UTS (Fig. 8(b)) is remarkably lower in the CA1.5 specimen due to the simultaneously lower YS (Fig. 8(b)) and poor work hardening response (Fig. 8(c) and Table 5), as compared to both CA0.0 and CA0.5 specimens.

Based on the above discussions, it can be summarized that the Ca content and thereby, the Ca/Al content ratio in the compositions play important roles in dictating the mechanical behaviour of the as-cast alloys by governing the microstructure and phase evolution in the

Mg–Al–Ca–Mn alloy. A lower Ca/Al ratio implies higher solubility of Al in the matrix, which culminates in better yield strength through solid solution strengthening. The formation of fine γ -Mg₁₇Al₁₂ particles also contribute to strengthening through particle-dislocation interactions in the specimen with lowest Ca/Al ratio. Despite the relative refinement of grain size, the higher Ca content and Ca/Al content ratio promote large fraction and strong networks of the hard and brittle Mg₂Ca phase. This eventually leads to poor ductility and work hardening response by facilitating the initiation and propagation of cracks in the specimens with higher Ca/Al ratios.

5. Conclusions

The role of Ca content and the Ca/Al ratio on the microstructure and phase evolution in lean as-cast Mg–Al–Ca–Mn alloys has been systematically examined in the present investigation. The Ca/Al content (expressed in wt.%) ratio has been specifically varied over a wide range of 0.06–2.21, where a maximum ratio of ~1.3 has been studied in the existing literature in this area. Further, the evolution of the second phases and the matrix phase in different alloy compositions, have also been estimated through thermodynamic calculations using Scheil conditions. Finally, the mechanical properties and the fracture behaviour of the different alloys have been studied and correlated to the microstructural developments. The notable conclusions drawn from this study are presented as follows.

- An increment in the Ca/Al content ratio from 0.06 to 2.21 led to a decrease in the solubility of Al in hcp Mg phase and thereby, in the lattice parameters ($a\sim 3.43$ to 3.12 \AA , $c\sim 5.6$ to 5.04 \AA) in the as-cast microstructure. This resulted in weakening of the matrix phase as reflected by the lower hardness (~80 VHN to ~46 VHN) and elastic modulus (~47 GPa–~42 GPa) of the matrix phase in specimens with higher Ca/Al content ratio.
- The dominant eutectic second phase changes according to the Ca/Al content ratio, from γ -Mg₁₇Al₁₂ phase in the CA0.0 specimen (Ca/Al ratio ~0.06) to C36-(Mg,Al)₂Ca phase in the CA0.5 specimen (Ca/Al ratio ~0.28) to C14-Mg₂Ca phase in the CA1.5 (Ca/Al ratio ~1.56) as well as CA2.0 (Ca/Al ratio ~2.21) specimens. The Al₈Mn₅ phase is observed to be present, albeit in small amount, in all the specimens.
- Increasing the Ca content and Ca/Al content ratio in the alloy composition resulted in significant rise in the area fraction (~2.1–7.2%) and network connectivity (fractal dimension ~1.11 to ~1.62) of the second phases. The higher area fraction of second phase restricted the grain growth during solidification and led to refinement of the grain size (~354 μm –161 μm).
- The refinement of grain size and increment of coarse second phase fraction resulted in the enhancement of microhardness in the alloy specimens (from ~35 to ~57 VHN) with increasing Ca/Al content ratio. However, the enhancement in the solid solution strengthening effect from higher solute concentration and the dislocation-pinning by the finer γ -Mg₁₇Al₁₂ phases resulted in better tensile properties (YS $\sim 130 \pm 5 \text{ MPa}$, UTS $\sim 183 \pm 9 \text{ MPa}$) in the CA0.0 specimen (Ca/Al content ratio ~0.06).
- Stronger connectivity of hard second phase resulting from a higher Ca content (1.28 and 1.66 wt%, respectively) and Ca/Al content ratio (~1.56 and ~2.21, respectively) in the as-cast CA1.5 and CA2.0 alloy specimens, resulted in poor ductility ($\leq 1.6\%$) and work hardening response. The larger differences in the hardness and elastic modulus between the matrix and the second phases signifies higher prestrained interface that facilitates initiation and propagation of cracks during tensile deformation in these specimens.

Data availability

The raw/processed data required to reproduce these findings cannot be shared at this time as the data also forms part of an ongoing study.

CRediT authorship contribution statement

S. Sanyal: Methodology, Investigation, Data curation, Formal analysis, Writing - original draft. **M. Paliwal:** Formal analysis, Writing - review & editing. **T.K. Bandyopadhyay:** Supervision, Validation, Writing - review & editing. **S. Mandal:** Conceptualization, Project administration, Resources, Supervision, Validation, Writing - review & editing.

Declaration of competing interest

The authors declare that they have no known competing financial interests or personal relationships that could have appeared to influence the work reported in this paper.

Acknowledgements

The authors are profoundly grateful to the National Facility for Atom Probe Tomography (NFAPT) at the Indian Institute of Technology Madras, Chennai, India for the 3DAP characterization of one of the specimens. The authors are also grateful to the Central Research Facility and the Department of Metallurgical and Materials Engineering at the Indian Institute of Technology Kharagpur, Kharagpur, India for providing with all the facilities required for all the other characterizations and analyses.

References

- [1] F. Briffod, T. Shiraiwa, M. Enoki, Monotonic and cyclic anisotropies of an extruded Mg–Al–Ca–Mn alloy plate: experiments and crystal plasticity studies, Mater. Sci. Eng. 772 (2020) 138753.
- [2] Q. Yang, S. Lv, P. Qin, F. Meng, X. Qiu, X. Hua, K. Guan, W. Sun, X. Liu, J. Meng, Interphase boundary segregation induced phase transformation in a high-pressure die casting Mg–Al–La–Ca–Mn alloy, Mater. Des. 190 (2020) 108566.
- [3] J.J. Bhattacharyya, T. Nakata, S. Kamado, S.R. Agnew, Origins of high strength and ductility combination in a Guinier-Preston zone containing Mg–Al–Ca–Mn alloy, Scripta Mater. 163 (2019) 121–124.
- [4] J.J. Bhattacharyya, T.T. Sasaki, T. Nakata, K. Hono, S. Kamado, S.R. Agnew, Determining the strength of GP zones in Mg alloy AXM10304, both parallel and perpendicular to the zone, Acta Mater. 171 (2019) 231–239.
- [5] H. Huang, H. Liu, C. Wang, J. Sun, J. Bai, F. Xue, J. Jiang, Potential of multi-pass ECAP on improving the mechanical properties of a high-calcium-content Mg–Al–Ca–Mn alloy, J. Magnes. Alloy. 7 (2019) 617–627.
- [6] T. Nakata, C. Xu, R. Ajima, Y. Matsumoto, K. Shimizu, T.T. Sasaki, K. Hono, S. Kamado, Improving mechanical properties and yield asymmetry in high-speed extrudable Mg-1.1Al-0.24Ca (wt %) alloy by high Mn addition, Mater. Sci. Eng. 712 (2018) 12–19.
- [7] Q. Huang, Y. Liu, M. Tong, H. Pan, C. Yang, T. Luo, Y. Yang, Enhancing tensile strength of Mg–Al–Ca wrought alloys by increasing Ca concentration, Vacuum (2020) 109356.
- [8] Y. Liu, N. Wang, J. Wang, B. Ma, D. Zhao, Investigation of the crystallographic structure and orientations of the Al₂Ca phase in a Mg–Al–Ca–Mn alloy, Mater. Char. 142 (2018) 377–382.
- [9] H. Pan, R. Kang, J. Li, H. Xie, Z. Zeng, Q. Huang, C. Yang, Y. Ren, G. Qin, Mechanistic investigation of a low-alloy Mg–Ca-based extrusion alloy with high strength-ductility synergy, Acta Mater. 186 (2020) 278–290.
- [10] B. Kondori, R. Mahmudi, Effect of Ca additions on the microstructure, thermal stability and mechanical properties of a cast AM60 magnesium alloy, Mater. Sci. Eng. 527 (2010) 2014–2021.
- [11] Y. Chai, B. Jiang, J. Song, Q. Wang, J. He, J. Zhao, G. Huang, Z. Jiang, F. Pan, Role of Al content on the microstructure, texture and mechanical properties of Mg-3.5Ca based alloys, Mater. Sci. Eng. 730 (2018) 303–316.
- [12] G. Han, D. Chen, G. Chen, J. Huang, Development of non-flammable high strength extruded Mg–Al–Ca–Mn alloys with high Ca/Al ratio, J. Mater. Sci. Technol. 34 (2018) 2063–2068.
- [13] S.W. Xu, S. Kamado, F. Uchida, T. Homma, K. Hono, High-strength extruded Mg–Al–Ca–Mn alloy, Scripta Mater. 65 (2011) 269–272.
- [14] T. Homma, S. Nakawaki, S. Kamado, Improvement in creep property of a cast Mg–6Al–3Ca alloy by Mn addition, Scripta Mater. 63 (2010) 1173–1176.
- [15] H. Pan, G. Qin, Y. Huang, Y. Ren, X. Sha, X. Han, Z.Q. Liu, C. Li, X. Wu, H. Chen, C. He, L. Chai, Y. Wang, J. feng Nie, Development of low-alloyed and rare-earth-free magnesium alloys having ultra-high strength, Acta Mater. 149 (2018) 350–363.
- [16] T. Nakata, T. Mezaki, C. Xu, K. Oh-Ishi, K. Shimizu, S. Hanaki, S. Kamado, Improving tensile properties of dilute Mg-0.27Al-0.13Ca-0.21Mn (at.%) alloy by low temperature high speed extrusion, J. Alloys Compd. 648 (2015) 429–437.

- [17] C. Wang, A. Ma, J. Sun, H. Liu, H. Huang, Z. Yang, Effect of ECAP process on as-cast and as-homogenized Mg-Al-Ca-Mn alloys with different Mg₂Ca morphologies, *J. Alloys Compd.* 793 (2019) 259–270.
- [18] N. Stanford, The effect of calcium on the texture, microstructure and mechanical properties of extruded Mg-Mn-Ca alloys, *Mater. Sci. Eng.* 528 (2010) 314–322.
- [19] A. Suzuki, N.D. Saddock, J.W. Jones, T.M. Pollock, Solidification paths and eutectic intermetallic phases in Mg-Al-Ca ternary alloys, *Acta Mater.* 53 (2005) 2823–2834.
- [20] L. Zhang, K. kun Deng, K. bo Nie, F. jun Xu, K. Su, W. Liang, Microstructures and mechanical properties of Mg-Al-Ca alloys affected by Ca/Al ratio, *Mater. Sci. Eng.* 636 (2015) 279–288.
- [21] Z.T. Li, X.G. Qiao, C. Xu, S. Kamado, M.Y. Zheng, A.A. Luo, Ultrahigh strength Mg-Al-Ca-Mn extrusion alloys with various aluminum contents, *J. Alloys Compd.* 792 (2019) 130–141.
- [22] H.A. Elamami, A. Incesu, K. Korgiopoulos, M. Pekguleryuz, A. Gungor, Phase selection and mechanical properties of permanent-mold cast Mg-Al-Ca-Mn alloys and the role of Ca/Al ratio, *J. Alloys Compd.* 764 (2018) 216–225.
- [23] S.M. Liang, R.S. Chen, J.J. Blandin, M. Sury, E.H. Han, Thermal analysis and solidification pathways of Mg-Al-Ca system alloys, *Mater. Sci. Eng.* 480 (2008) 365–372.
- [24] Z.T. Li, X.D. Zhang, M.Y. Zheng, X.G. Qiao, K. Wu, C. Xu, S. Kamado, Effect of Ca/Al ratio on microstructure and mechanical properties of Mg-Al-Ca-Mn alloys, *Mater. Sci. Eng.* 682 (2017) 423–432.
- [25] M. Zubair, S. Sandlöbes, M.A. Wollenweber, C.F. Kusche, W. Hildebrandt, C. Broeckmann, S. Korte-Kerzel, On the role of Laves phases on the mechanical properties of Mg-Al-Ca alloys, *Mater. Sci. Eng.* 756 (2019) 272–283.
- [26] Z.T. Li, X.G. Qiao, C. Xu, S. Kamado, M.Y. Zheng, A.A. Luo, Ultrahigh strength Mg-Al-Ca-Mn extrusion alloys with various aluminum contents, *J. Alloys Compd.* 792 (2019) 130–141.
- [27] B.D. Cullity, Elements of X-Ray Diffraction, Addison-Wesley Publishing Company, Inc., Reading, Massachusetts, USA, 1956.
- [28] M.U. Cohen, Precision lattice constants from x-ray powder photographs, *Rev. Sci. Instrum.* 6 (1935) 68–74.
- [29] P. Duley, S. Sanyal, T.K. Bandyopadhyay, S. Mandal, Implications of grain size distribution, precipitate evolution and texture development on tensile properties in hard plate hot forged and annealed Mg-Zn-Ca-Mn alloy, *Mater. Sci. Eng. A* 784 (2020) 139288.
- [30] P. Duley, S. Sanyal, T.K. Bandyopadhyay, S. Mandal, Homogenization-induced age-hardening behavior and room temperature mechanical properties of Mg-4Zn-0.5Ca-0.16Mn (wt%) alloy, *Mater. Des.* 164 (2019) 107554.
- [31] M.B. Dillencourt, H. Samet, M. Tamminen, A general approach to connected-component labeling for arbitrary image representations, *J. Assoc. Comput. Mach.* 39 (1992) 253–280.
- [32] S.K. Pradhan, T.S. Prithiv, S. Mandal, Through-thickness microstructural evolution during grain boundary engineering type thermomechanical processing and its implication on sensitization behavior in austenitic stainless steel, *Mater. Char.* 134 (2017) 134–142.
- [33] S.K. Pradhan, P. Bhuyan, S. Mandal, Individual and synergistic influences of microstructural features on intergranular corrosion behavior in extra-low carbon type 304L austenitic stainless steel, *Corrosion Sci.* 139 (2018) 319–332.
- [34] S. Kobayashi, R. Kobayashi, T. Watanabe, Control of grain boundary connectivity based on fractal analysis for improvement of intergranular corrosion resistance in SUS316L austenitic stainless steel, *Acta Mater.* 102 (2016) 397–405.
- [35] E. Charkaluk, M. Bigerelle, A. Iost, Fractals and fracture, *Eng. Fract. Mech.* 61 (1998) 119–139.
- [36] T.S. Prithiv, P. Bhuyan, S.K. Pradhan, V. Subramanya Sarma, S. Mandal, A critical evaluation on efficacy of recrystallization vs. strain induced boundary migration in achieving grain boundary engineered microstructure in a Ni-base superalloy, *Acta Mater.* 146 (2018) 187–201.
- [37] C.W. Bale, E. Béolis, P. Chartrand, S.A. Decterov, G. Eriksson, A.E. Gheribi, K. Hack, I.H. Jung, Y.B. Kang, J. Melançon, A.D. Pelton, S. Petersen, C. Robelin, J. Sangster, P. Spencer, M.A. Van Ende, FactSage thermochemical software and databases, 2010–2016, *Calphad Comput. Coupling Phase Diagrams Thermochem* 54 (2016) 35–53.
- [38] P. Liang, T. Tarfa, J.A. Robinson, S. Wagner, P. Ochin, M.G. Harmelin, H.J. Seifert, H.L. Lukas, F. Aldinger, Experimental investigation and thermodynamic calculation of the Al-Mg-Zn system, *Thermochim. Acta* 314 (1998) 87–110.
- [39] A. Kozlov, M. Ohno, R. Arroyave, Z.K. Liu, R. Schmid-Fetzer, Phase equilibria, thermodynamics and solidification microstructures of Mg-Sn-Ca alloys, Part 1: experimental investigation and thermodynamic modeling of the ternary Mg-Sn-Ca system, *Intermetallics* 16 (2008) 299–315.
- [40] J. Gröbner, D. Mirkovic, M. Ohno, R. Schmid-Fetzer, Experimental investigation and thermodynamic calculation of binary Mg-Mn phase equilibria, *J. Phase Equilibria Diffus.* 26 (2005) 234–239.
- [41] D. Kevorkov, R. Schmid-Fetzer, A. Pisch, F. Hodaj, C. Colinet, The Al-Ca system, Part 2: calorimetric measurements and thermodynamic assessment, *Zeitschrift Fuer Met* 92 (2001) 953–958.
- [42] Y. Du, J. Wang, J. Zhao, J.C. Schuster, F. Weitzer, R. Schmid-Fetzer, M. Ohno, H. Xu, Z.K. Liu, S. Shang, W. Zhang, Reassessment of the Al-Mn system and a thermodynamic description of the Al-Mg-Mn system, *Int. J. Mater. Res.* 98 (2007) 855–871.
- [43] A. Janz, Thermodynamics and Constitution of Quaternary Mg-Al-Ca-Sr Alloys and the Extension to the Quinary Mg-Al-Ca-Sr-Mn System, TU Clausthal, 2008.
- [44] A. Janz, J. Gro, H. Cao, J. Zhu, Y.A. Chang, R. Schmid-fetzer, Thermodynamic modeling of the Mg-Al-Ca system, *Acta Mater.* 57 (2009) 682–694.
- [45] G. Zeng, J.W. Xian, C.M. Gourlay, Nucleation and growth crystallography of Al₈Mn₅ on B2-Al(Mn,Fe) in AZ91 magnesium alloys, *Acta Mater.* 153 (2018) 364–376.
- [46] G. Zeng, X. Zhu, S. Ji, C.M. Gourlay, The morphology and distribution of Al₈Mn₅ in high pressure die cast AM50 and AZ91, in: D. Orlov, V. Joshi, K.N. Solanki, N. Neelamegham (Eds.), *Magnes. Technol.*, Springer, 2018, pp. 137–144.
- [47] S. Mandal, K.G. Pradeep, S. Zaeferrer, D. Raabe, A novel approach to measure grain boundary segregation in bulk polycrystalline materials in dependence of the boundaries' five rotational degrees of freedom, *Scripta Mater.* 81 (2014) 16–19.
- [48] H. Zhang, K.G. Pradeep, S. Mandal, D. Ponge, D. Raabe, New insights into the austenitization process of low-alloyed hypereutectoid steels: nucleation analysis of strain-induced austenite formation, *Acta Mater.* 80 (2014) 296–308.
- [49] H. Zhang, H. Wang, J. Wang, J. Rong, M. Zha, C. Wang, P. Ma, Q. Jiang, The synergy effect of fine and coarse grains on enhanced ductility of bimodal-structured Mg alloys, *J. Alloys Compd.* 780 (2019) 312–317.
- [50] A.D. Rollett, U.F. Kocks, A review of the stages of work hardening, *Solid State Phenom.* 35–36 (1993) 1–18.
- [51] H.Y. Wu, F.Z. Lin, Mechanical properties and strain-hardening behavior of Mg alloy AZ31B-H24 thin sheet, *Mater. Sci. Eng.* 527 (2010) 1194–1199.
- [52] S. Sanyal, S. Kanodia, R. Saha, T.K. Bandyopadhyay, S. Mandal, Influence of hard plate hot forging temperature on the microstructure, texture and mechanical properties in a lean Mg-Zn-Al alloy, *J. Alloys Compd.* 800 (2019) 343–354.
- [53] S.S. Nene, S. Zellner, B. Mondal, M. Komarasamy, R.S. Mishra, R.E. Brennan, K. C. Cho, Friction stir processing of newly-designed Mg-5Al-3.5Ca-1Mn (AXM541) alloy: microstructure evolution and mechanical properties, *Mater. Sci. Eng.* 729 (2018) 294–299.
- [54] A. Suzuki, N.D. Saddock, J.W. Jones, T.M. Pollock, Structure and transition of eutectic (Mg,Al)₂Ca laves phase in a die-cast Mg-Al-Ca base alloy, *Scripta Mater.* 51 (2004) 1005–1010.
- [55] S. Chatterjee, S. Chabri, H. Chakraborty, N. Bhowmik, A. Sinha, Micromechanical and nanoscratch behavior of SiCp dispersed metal matrix composites, *J. Mater. Eng. Perform.* 24 (2015) 3407–3418.
- [56] N.K. Mukhopadhyay, P. Paufler, Micro- and nanoindentation techniques for mechanical characterisation of materials, *Int. Mater. Rev.* 51 (2006) 209–245.
- [57] E.O. Hall, The deformation and ageing of mild steel: III Discussion of results, *Proc. Phys. Soc. B* 64 (1951) 747–753.
- [58] N.J. Petch, The cleavage strength of polycrystals, *J. Iron Steel Inst.* 173 (1953) 25–28.
- [59] N. Hansen, B. Ralph, The strain and grain size dependence of the flow stress of copper, *Acta Metall.* 30 (1982) 411–417.
- [60] Z.C. Cordero, B.E. Knight, C.A. Schuh, Six decades of the Hall-Petch effect - a survey of grain-size strengthening studies on pure metals, *Int. Mater. Rev.* 61 (2016) 495–512.
- [61] C.H. Caceres, G.E. Mann, J.R. Griffiths, Grain size hardening in Mg and Mg-Zn solid solutions, *Metall. Mater. Trans.* 42 (2011) 1950–1959.
- [62] R.L. Fleischer, Substitutional solution hardening, *Acta Metall.* 11 (1963) 203–209.
- [63] R.L. Fleischer, Substitutional solutes in AlRu-II. Hardening and correlations with defect structure, *Acta Metall.* 41 (1993) 1197–1205.
- [64] R.L. Fleischer, The Strengthening of Metals, Reinhold Press, New York, 1964.
- [65] J.H. Shen, Y.L. Li, Q. Wei, Statistic derivation of Taylor factors for polycrystalline metals with application to pure magnesium, *Mater. Sci. Eng.* 582 (2013) 270–275.
- [66] C.A. Schuh, T.G. Nieh, H. Iwasaki, The effect of solid solution W additions on the mechanical properties of nanocrystalline Ni, *Acta Mater.* 51 (2003) 431–443.
- [67] H.F. Sun, C.J. Li, Y. Xie, W. Bin Fang, Microstructures and mechanical properties of pure magnesium bars by high ratio extrusion and its subsequent annealing treatment, *Trans. Nonferrous Met. Soc. China (English Ed.)* 22 (2012) s445–s449.
- [68] G.E. Dieter, D. Bacon, Mechanical Metallurgy, third ed., McGraw Hill Book Company, London, 1988.
- [69] Z.W. Huang, Y.H. Zhao, H. Hou, Y.H. Zhao, X.F. Niu, P. De Han, Structural, thermodynamics and elastic properties of Mg₁₇Al₁₂, Al₂Y and Al₄Ba phases by first-principles calculations, *J. Cent. South Univ. Technol.* 19 (2012) 1475–1481.
- [70] G. Zhu, L. Wang, J. Wang, J. Park, X. Zeng, Highly deformable Mg-Al-Ca alloy with Al₂Ca precipitates, *Acta Mater.* 200 (2020) 236–245.